NAVAL POSTGRADUATE SCHOOL

MONTEREY, CALIFORNIA

THESIS

DETERMINING THE FINE STRUCTURE OF THE ENTRAINMENT ZONE IN CLOUD-TOPPED BOUNDARY LAYERS

by

Michael S. Horner

March 2005

Thesis Advisor:	Qing Wang
Second Reader:	Carlyle H. Wash

Approved for public release; distribution is unlimited.

THIS PAGE INTENTIONALLY LEFT BLANK

REPORT DOCUMENTATION PAGE	*Form Approved OMB No. 0704-0188*

Public reporting burden for this collection of information is estimated to average 1 hour per response, including the time for reviewing instruction, searching existing data sources, gathering and maintaining the data needed, and completing and reviewing the collection of information. Send comments regarding this burden estimate or any other aspect of this collection of information, including suggestions for reducing this burden, to Washington headquarters Services, Directorate for Information Operations and Reports, 1215 Jefferson Davis Highway, Suite 1204, Arlington, VA 22202-4302, and to the Office of Management and Budget, Paperwork Reduction Project (0704-0188) Washington DC 20503.

1. AGENCY USE ONLY *(Leave blank)*	**2. REPORT DATE** March 2005	**3. REPORT TYPE AND DATES COVERED** Master's Thesis

4. TITLE AND SUBTITLE: Determining the Fine Structure of the Entrainment Zone in Cloud-Topped Boundary Layers	**5. FUNDING NUMBERS**
6. AUTHOR(S) Michael S. Horner	
7. PERFORMING ORGANIZATION NAME(S) AND ADDRESS(ES) Naval Postgraduate School Monterey, CA 93943-5000	**8. PERFORMING ORGANIZATION REPORT NUMBER**
9. SPONSORING /MONITORING AGENCY NAME(S) AND ADDRESS(ES) N/A	**10. SPONSORING/MONITORING AGENCY REPORT NUMBER**

11. SUPPLEMENTARY NOTES The views expressed in this thesis are those of the author and do not reflect the official policy or position of the Department of Defense or the U.S. Government.

12a. DISTRIBUTION / AVAILABILITY STATEMENT Approved for public release; distribution is unlimited.	**12b. DISTRIBUTION CODE**

13. ABSTRACT (maximum 200 words)

The objective of this thesis is to obtain a better understanding of cloud-top entrainment through an in-depth analysis of entrainment-zone structure. *In situ* aircraft measurements taken during the Atlantic Stratocumulus Transition Experiment (ASTEX) were used for this purpose. Using data collected from multiple cloud-top penetrations, the presence of an interfacial layer in-between the top of the cloud mixed-layer and the base of the free atmosphere is identified and consequently defined as the entrainment zone. The depth of the entrainment zone is on the order of tens of meters, where turbulence and sometimes cloud droplets are detectable. Inhomogeneous mixing was found to occur within the entrainment zone. Parcels of inversion-layer air and boundary-layer air are identified within the entrainment zone. Analyses suggest that turbulence intensity and cloud amount in the entrainment zone vary depending on the distribution of entrainment mixing fraction. Furthermore, continuous mixing in the entrainment zone appears to dissipate the upper-cloud layer. However, continuous dissipation of the upper-cloud layer has not been observed. Further study is needed to determine the interaction between cloud-top entrainment and the full integration of boundary-layer dynamics.

14. SUBJECT TERMS Cloud-top entrainment, Entrainment-zone structure, Aircraft measurements, ASTEX, Entrainment zone, Inhomogeneous mixing, Entrainment mixing fraction	**15. NUMBER OF PAGES** 93
	16. PRICE CODE

17. SECURITY CLASSIFICATION OF REPORT Unclassified	**18. SECURITY CLASSIFICATION OF THIS PAGE** Unclassified	**19. SECURITY CLASSIFICATION OF ABSTRACT** Unclassified	**20. LIMITATION OF ABSTRACT** UL

NSN 7540-01-280-5500 Standard Form 298 (Rev. 2-89)
Prescribed by ANSI Std. 239-18

THIS PAGE INTENTIONALLY LEFT BLANK

Approved for public release; distribution is unlimited

DETERMINING INVERSION STRUCTURE AT THE TOP OF THE PLANETARY BOUNDARY LAYER

Michael S. Horner
Captain, United States Air Force
B.S., University of South Alabama, 2000

Submitted in partial fulfillment of the
requirements for the degree of

MASTER OF SCIENCE IN METEOROLOGY

from the

NAVAL POSTGRADUATE SCHOOL
March 2005

Author: Michael S. Horner

Approved by: Qing Wang
Thesis Advisor

Carlyle H. Wash
Second Reader/Co-Advisor

Philip A. Durkee
Chairman, Department of Meteorology

THIS PAGE INTENTIONALLY LEFT BLANK

ABSTRACT

The objective of this thesis is to obtain a better understanding of cloud-top entrainment through an in-depth analysis of entrainment-zone structure. *In situ* aircraft measurements taken during the Atlantic Stratocumulus Transition Experiment (ASTEX) were used for this purpose. Using data collected from multiple cloud-top penetrations, the presence of an interfacial layer in-between the top of the cloud mixed-layer and the base of the free atmosphere is identified and consequently defined as the entrainment zone. The depth of the entrainment zone is on the order of tens of meters, where turbulence and sometimes cloud droplets are detectable. Inhomogeneous mixing was found to occur within the entrainment zone. Parcels of inversion-layer air and boundary-layer air are identified within the entrainment zone. Analyses suggest that turbulence intensity and cloud amount in the entrainment zone vary depending on the distribution of entrainment mixing fraction. Furthermore, continuous mixing in the entrainment zone appears to dissipate the upper-cloud layer. However, continuous dissipation of the upper-cloud layer has not been observed. Further study is needed to determine the interaction between cloud-top entrainment and the full integration of boundary-layer dynamics.

THIS PAGE INTENTIONALLY LEFT BLANK

TABLE OF CONTENTS

THIS PAGE INTENTIONALLY LEFT BLANK

LIST OF FIGURES

LIST OF TABLES

THIS PAGE INTENTIONALLY LEFT BLANK

ACKNOWLEDGMENTS

I would like to thank my advisor, Professor Qing Wang, for her mentorship and guidance throughout the development of this thesis. Her insights on boundary-layer structure and entrainment were the backbone of this study. Additionally, I would like to thank Professor Chuck Wash for his encouragement and assistance as the second reader of this thesis.

I would also like to thank the following people: Capt Daniel Weekley (for inspiring me to embark upon a career in Meteorology), Dr. Keith Blackwell, of the Department of Earth Sciences, University of South Alabama (for laying the foundation of my meteorological knowledge base), Captains Daniel Weekley and Robb Randall (for encouraging me to pursue postgraduate education), and Dr. Lisa Chang, an Exchange Scholar from Taiwan (for her data retrieval and computer programming assistance during this endeavor).

I also want to express the utmost gratitude to my wife, Georgia, and our children, Michael, Logan, and Liberty, for their loving support and patience during the writing of this thesis.

THIS PAGE INTENTIONALLY LEFT BLANK

I. INTRODUCTION

A. MILITARY SIGNIFICANCE AND THESIS OBJECTIVES

US military personnel need to be familiar with the battlespace environment. They must understand how atmospheric conditions impact our operations and the operations of our adversaries, and to use this knowledge to our benefit. Proper battlespace planning requires taking nothing less than full advantage of the environment.

Despite ongoing efforts to develop all-weather capabilities, atmospheric conditions still constrain military operations and systems. As military technology becomes progressively more sophisticated, both systems and operations will be increasingly influenced by atmospheric variability. Sensor and weapon system developers must understand environmental effects on system performance in order to optimize design effectiveness, and commanders need to know which atmospheric conditions are favorable or restrictive to military operations (Bach and Harmon 1999).

The primary theater for a multitude of military operations is the planetary boundary layer. To begin with, humanity resides within the boundary layer. Secondly, all near-ground operations are conducted here. A vast number of military concerns lie within this relatively small portion of the atmosphere. Daily weather forecasts for fog, frost, pollution, and maximum and minimum temperatures are really boundary-layer forecasts (Stull 1988, p. 21).

Most aircraft fly above the boundary layer en route to their destination. However, they must pass through the boundary layer upon takeoff and landing (Lenschow 1986, p. 39). This layer of the atmosphere is intensely turbulent, making it a potential hazard to aviation. Thus, knowledge about the structure of the boundary layer is relevant to the needs of Air Force aviation.

The Air Force also heavily depends on the propagation of electromagnetic and acoustic signals through the boundary layer for reconnaissance, detection and ranging, and the operation of smart munitions. The quick detection, identification, and quantification of chemical and biological agents, in addition to natural and induced aerosols, requires a thorough understanding of boundary-layer effects on sensors. For example, turbulence can severely impact the performance of optical sensors, infrared imaging equipment, and acoustic detection systems by affecting the propagation, sensing, and coherence of transmitted and received signals through the boundary layer (Bach and Harmon 1999).

The major objectives of this thesis are to characterize the entrainment zone using fine-scale aircraft measurements, and to understand the role of cloud-top entrainment on cloud evolution. Cloud-top parameterizations for numerical models can be further developed through a better understanding of the entrainment zone. This study begins with an introduction on the planetary boundary layer and the role of entrainment at the cloud top. An overview of the Atlantic Stratocumulus Transition Experiment (ASTEX), a field survey which focused on key boundary-layer processes, is presented next. This is followed by an analysis of the data collected during ASTEX and used in this thesis. Key findings from this research are presented and deliberated upon next. Lastly, this study concludes with the implications of these findings and recommendations for future studies.

B. THE BOUNDARY LAYER

The surface of the earth acts as a boundary on the domain of the atmosphere. This constraint results in a distinct atmospheric stratum known as the planetary boundary layer (see Figure 1). It is defined as “…that part of the troposphere that is directly influenced by the presence of the earth’s surface…” (Stull 1988, p. 2). The boundary layer comprises the lowest 100 to 3000 meters of the atmosphere. The air in the troposphere above the boundary layer is referred to as the free atmosphere because it “…behaves as if there were no boundary to contend with…” (Stull 1988, p. 5). Separating these two layers of the troposphere is a region of transition known as the entrainment zone.

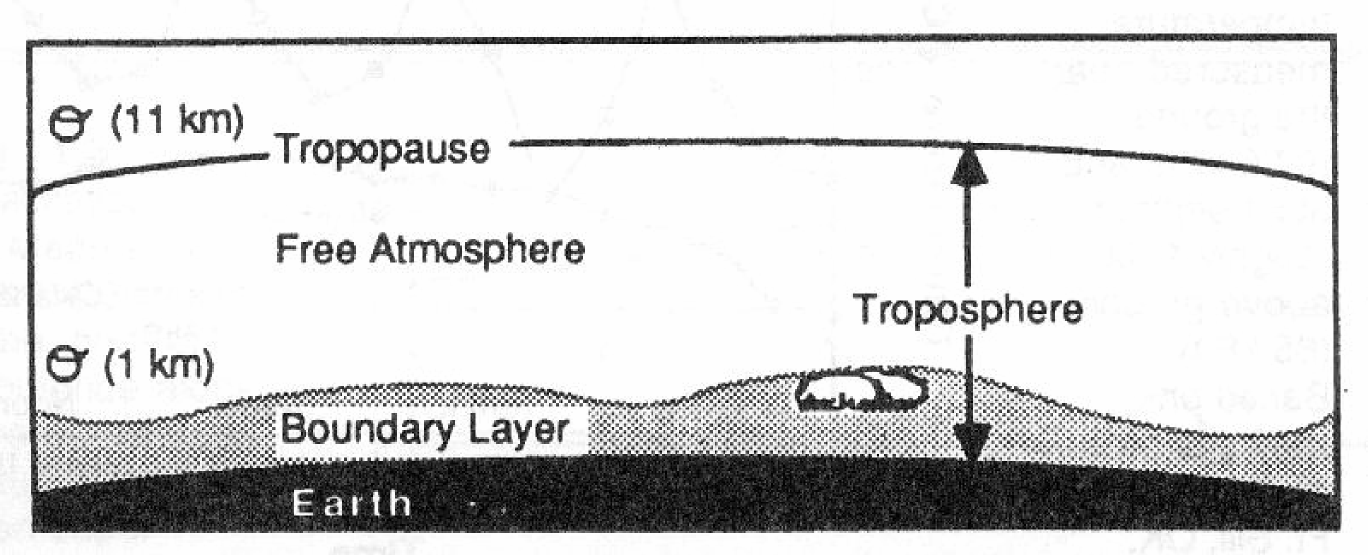

Figure 1. The troposphere can be divided into two parts: A boundary layer near the surface and the free atmosphere above it (From Stull 1988, p. 1).

The boundary layer is characterized by turbulence. Much of this turbulence is caused by forcings from the surface. For example, solar heating of the ground generates thermals of rising air. These thermals consist of irregular swirls of motion known as eddies. Another common source of turbulence comes from wind shear. Obstacles such as mountains and buildings also contribute to turbulence by deflecting the mean wind flow and producing turbulent wakes adjacent to and downstream of the obstacle. Because turbulence is so pervasive in this region, it is often used to *define* the boundary layer (Stull 1988, p. 3).

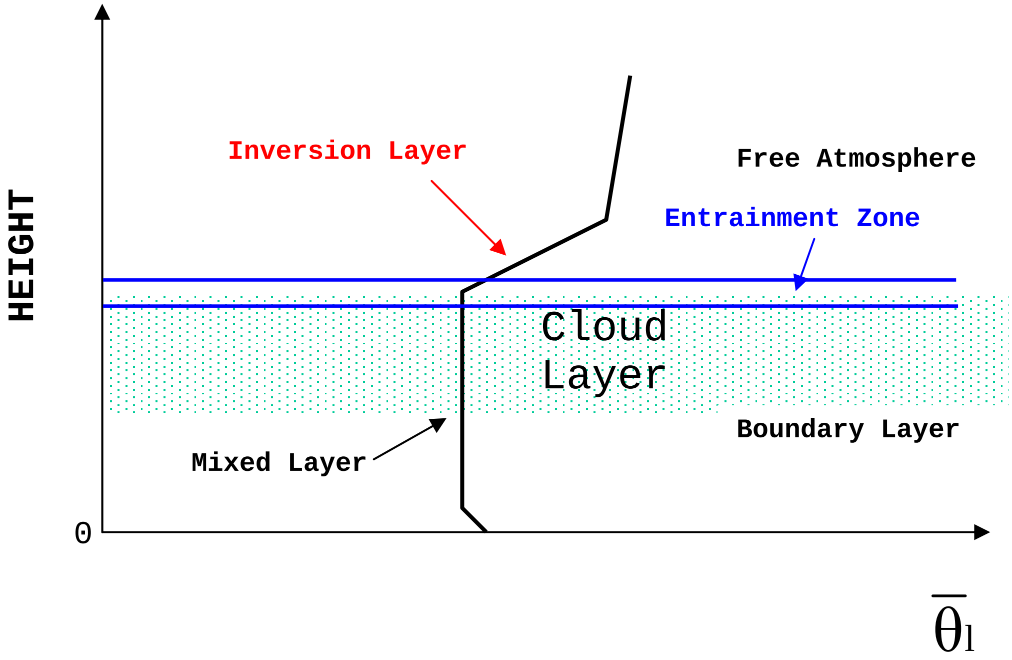

Figure 2. Typical profile of mean liquid water potential temperature. The mixed layer is capped by stable air in the inversion layer. Entrainment occurs at the bottom of the inversion layer and the top of the mixed layer (After Stull 1988, p. 13).

Turbulent motion results in a well-mixed layer within the boundary layer (see Figure 2). Turbulence blends heat, moisture, and momentum nearly uniformly in the vertical. As a result of this mixing, atmospheric constituents remain virtually constant with height. Air parcels lifted to their lifting condensation level (LCL) will condense and form clouds at the top of the mixed layer. A stable layer of air caps the top of the cloud-mixed layer, which acts as a lid on rising thermals, thereby limiting the domain of turbulence (Stull 1988, p. 13).

1. Entrainment

The stable layer located above the mixed layer is often strong enough to be classified as a temperature inversion. Air temperature can increase appreciably with height in this region. Located near the base of the inversion layer is an interfacial layer known as the entrainment zone. This transitional region is referred to as the entrainment zone because air from the free atmosphere is drawn down, or entrained, into the boundary layer below. The entrainment zone can also be characterized as a layer of intermittent turbulence and overshooting thermals at the top of the mixed layer (see Figure 3).

The terms inversion layer and entrainment zone are sometimes used synonymously, but Figure 2 illustrates that they are two distinct regions. Entrainment is not confined solely to the inversion layer. However, there is a correlation between the two. The entrainment zone is thinner when a strong temperature inversion caps the boundary layer, and thicker when thermals and turbulence are more dynamic under a weak temperature inversion (Glickman 2000, p. 268).

At its thickest, the entrainment zone can average 40% of the depth of the mixed layer. The top of the entrainment zone is defined by the top of the highest overshooting thermal within it. The bottom of the entrainment zone cannot be so easily determined. A sharp demarcation, indicating where entrainment ends, does not exist. Thus, for research purposes, the bottom is normally delineated at a height where approximately 5-10% of the air on a horizontal plane has the characteristics of free-atmosphere air (Stull 1988, p. 473).

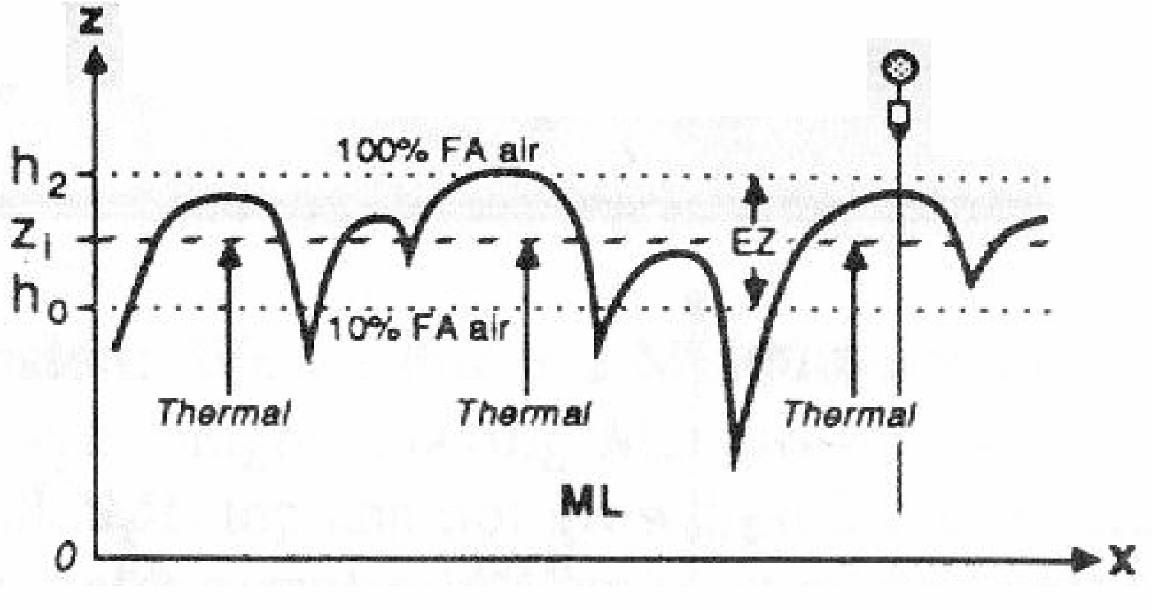

Figure 3. The entrainment zone (EZ) can be defined in terms of the amount of free-atmosphere (FA) air present. h_2 indicates the top of the entrainment zone, while h_0 represents the bottom. The top of the mixed layer (ML) is represented by the solid line; z_i indicates the average height of the ML top (From Stull 1988, p. 474).

2. Cloud-topped Boundary Layers

The two individual cloud types most often observed during boundary-layer studies are cumulus and stratocumulus (Wang and Lenschow 1995). Cumulus clouds are formed by convection in unstable air. As thermals rise, they cool by adiabatic expansion and mixing. When the rising air cools to its saturation point, condensation occurs, and the thermals become visible as cumulus clouds (Ahrens 1994, p. 175). The mixing of a moist layer of stable air produces stratocumulus clouds (Ahrens 1994, pp. 175-185).

These two cloud types represent the major regimes encountered along a trade wind trajectory, which traverses over progressively warmer sea surface temperatures (SSTs). At the upwind end of the trajectory (farther poleward), extensive sheets of low-level stratocumulus develop over relatively cool water off the west coast of continents. Downwind (closer to the equator), fields of cumulus form in a substantially deeper boundary layer. Stratocumulus-topped boundary layers are shallower, possess greater cloud coverage, and are capped by a strong inversion. In contrast, cumulus-topped boundary layers have weaker capping inversions and are found in weaker subsidence regions (Wang and Lenschow 1995). A typical cloud coverage amount for trade cumulus clouds is 20%-30% (Warren et al. 1989). By comparison, stratocumulus cloud amounts (see Figure 4) can comprise over 80% of the total cloud amount (Randall 2004).

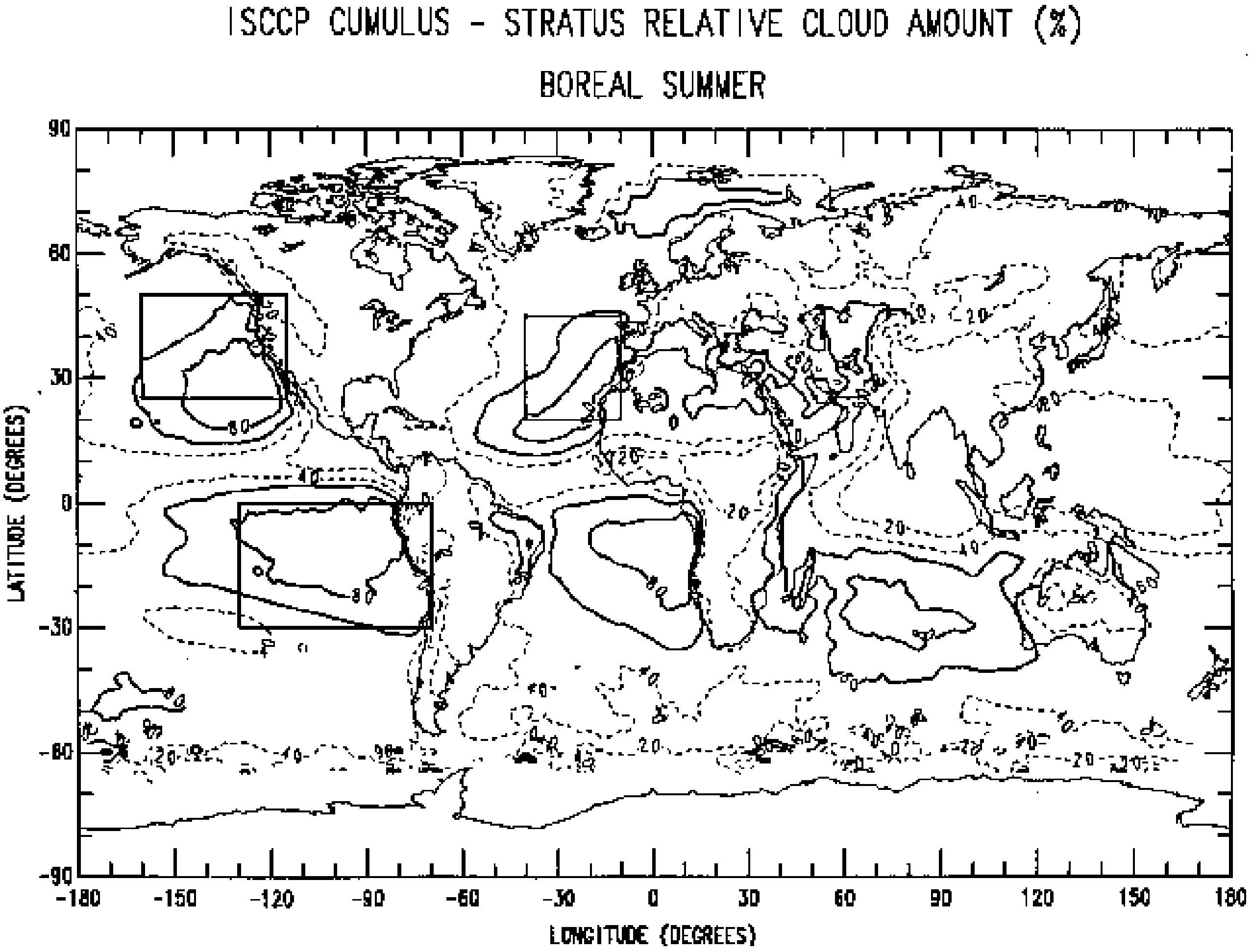

ISCCP CUMULUS - STRATUS RELATIVE CLOUD AMOUNT (%)

BOREAL SUMMER

Figure 4. Geographic distribution of mean cumulus-stratus cloud amount relative to total cloud amount during the summer months, from Randall (2004). Bold contours indicate regions where >50% and >80% of the clouds are marine stratocumulus. Rectangles indicate where major marine stratocumulus studies have been conducted.

Marine boundary-layer clouds have a large impact on the shortwave radiation budget due to their high albedo and somewhat ubiquitous nature. Conversely, they have only a minimal effect on the longwave radiation budget because their cloud-top temperatures are only slightly cooler than the underlying ocean surface. Thus, they cool the surface of the ocean by restricting insolation, while allowing sea-surface longwave losses to space. As a consequence of their radiative effects over large areas and on long timescales in the tropics and subtropics, they must be duly accounted for in numerical models.

Accurately parameterizing marine boundary-layer clouds has proven to be a daunting task due to the complex structure of the clouds, which exhibit great variability across a broad range of spatial and temporal scales. There is a lot of uncertainty about the interaction between oceans, radiation, and clouds. Small biases in marine boundary-layer cloud representations can yield substantial errors in the simulated local radiation balance (Kogan et al. 1995). Thus, a better understanding of boundary-layer clouds is needed.

One of the important factors in determining the structure and evolution of these clouds is the role of entrainment at the cloud top (Lenschow et al. 2000). Entrainment continually lifts the cloud top, maintaining it against large-scale subsidence, but it also dries out the boundary layer. Cloud structure in the boundary layer is sensitive to turbulence, creating a feedback on entrainment rate. This feedback helps regulate a constantly changing balance between cloud composition, entrainment, and turbulence (Bretherton et al. 2004).

This thesis attempts to identify the processes that govern cloud-top entrainment. Data retrieved from ASTEX was utilized for this study. A brief overview of this field experiment, and how the data was obtained, follows.

THIS PAGE INTENTIONALLY LEFT BLANK

II. TECHNIQUE

A. OVERVIEW OF ASTEX

Cloud-topped boundary layers have been the focus of numerous field experiments from which a great deal has been learned. One of the most ambitious of these experiments was a cloud study known as the First International Satellite Cloud Climatology Project Regional Experiment (FIRE) (Albrecht et al. 1988). However, this study did not include broken stratocumulus clouds and deep boundary layers, which are an important intermediate step in the breakup of stratocumulus to trade cumulus clouds. Therefore, ASTEX was undertaken to provide an improved understanding of the processes that govern the transition to broken cloud conditions, and the processes that influence cloud type and amount (Albrecht et al. 1995).

ASTEX was conducted during the summer of 1992 (1-28 June) off the northwest African coast, in the vicinity of the Azores and Madeira Islands (Figure 5). This region is dominated by intermittent low-level cloudiness with cloud conditions ranging from solid stratocumulus decks to broken trade cumuli. Continental effects do not directly influence this oceanic area, and islands make convenient places to perform surface observations and to conduct aircraft operations (Randall 1995). Thus, this region was an ideal test bed for the ASTEX study.

Several observational platforms were used during ASTEX: aircraft, ships, satellites, and surface-based stations. A telescoping approach was used to examine scales of motion ranging from the cloud scale (microns) to the synoptic scale (thousands of kilometers). Satellite imagery and upper-level aircraft provided a description of large-scale atmospheric features, while specially equipped aircraft flying in the boundary layer and surface-based remote sensors provided information on the microphysical properties of low-level clouds. Satellite data was collected from METEOSAT, NOAA Polar Orbiter, Landsat, SPOT, and DMSP satellites. Extensive suites of instruments were deployed on Porto Santo, one of the Madeira Islands, and the island of Santa Maria in the Azores. Observations taken from these islands and oceanic research vessels provided surface meteorological conditions, surface radiative fluxes, and upper-air data, which assisted with the large-scale assessment of the atmosphere.

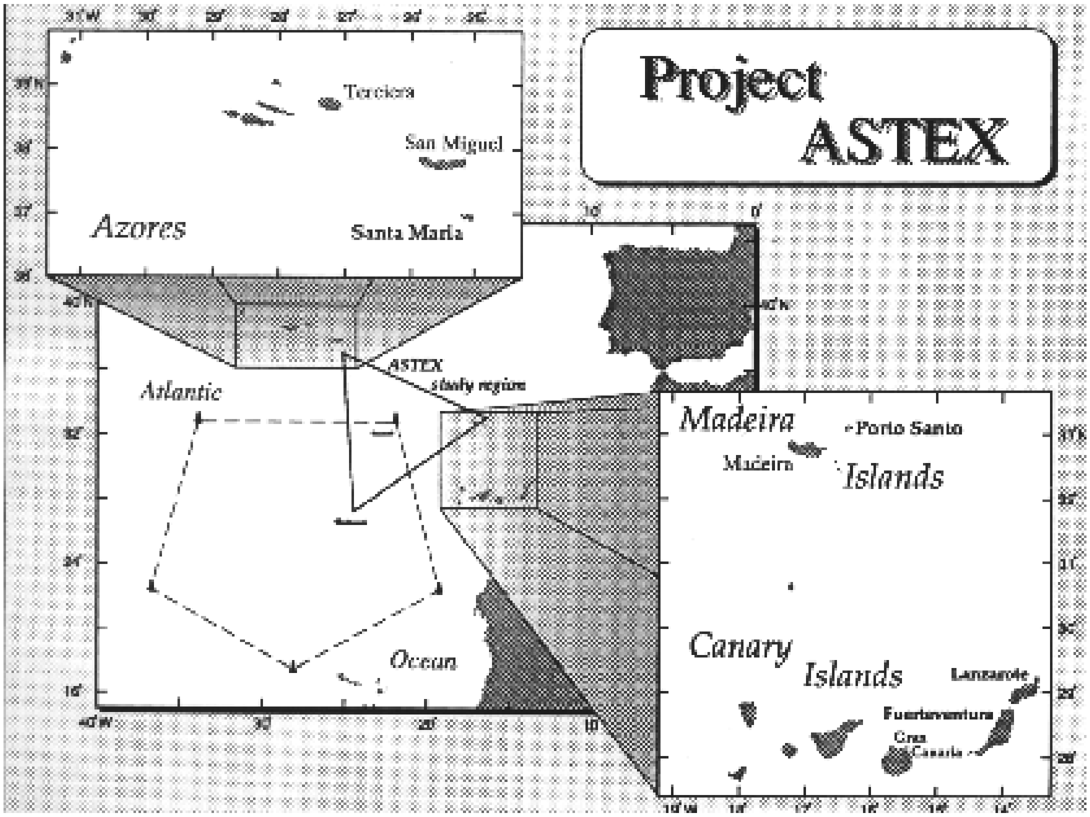

Figure 5. ASTEX study region (From Albrecht et al. 1995).

ASTEX was part of a large multinational collaboration. It consisted of more than 200 scientists, students, and support staff from the United States, United Kingdom, France, Germany, Portugal, the Netherlands, Russia, and Spain. The Office of Naval Research sponsored ASTEX with strong support from NASA, NSF, NOAA, and DOE.

From a broad perspective, ASTEX was intended to improve dynamical, radiative, and microphysical models. An increased understanding of aerosols, cloud microphysics, and chemistry on large-scale cloud properties was also desired so that parameterizations for regional and climate models could be further developed. One of the key processes ASTEX was specifically designed for was the analysis of cloud-top entrainment.

The ASTEX project was highly successful, due in large part to favorable weather. A subtropical high provided the conditions necessary to support substantial low-level cloud coverage. Two major highlights of the ASTEX field deployment include a generous sampling of boundary-layer cloud regions and a successful demonstration of the Lagrangian approach. The results of ASTEX generated unparalleled insight into the formation, maintenance, and dissipation of boundary-layer clouds and their parameterizations in regional and general circulation models (Albrecht et al. 1995). Analysis of the data obtained during ASTEX continues to clarify our understanding of the boundary layer to this day.

B. LAGRANGIAN STRATEGY

Few observations in meteorology are Lagrangian. Rather, the vast majority of meteorological observations are made in Eulerian coordinates. In the Eulerian system, "…properties of a fluid are assigned to points in space at each given time, without attempt[ing] to identify individual fluid parcels from one time to the next” (Glickman 2000, p. 281). A sequence of synoptic charts is an example of the Eulerian method for representing data. The Lagrangian system differs from the Eulerian system in that Lagrangian coordinates do not vary with time. This method allows for the tracking of one parcel of air along its trajectory. Measurements taken with the aid of constant-pressure balloons are a common way in which Lagrangian observations are made (Glickman 2000, p. 439).

The Lagrangian method used during ASTEX was designed to follow and inclusively measure cloud evolution and the physical and chemical processes in a single boundary-layer airmass. During the two Lagrangian intensive observation periods (IOPs), a column of air within a convecting mixed layer (ML) was tracked for 36-48 hours. The two Lagrangian IOPs took place between 1600 UTC 12 June - 1200 UTC 14 June and 2200 UTC 18 June – 1400 UTC 20 June, 1992 (Bretherton and Pincus 1995). Nearly nonstop aircraft coverage by three boundary-layer airplanes, supplemented by satellite and ship observations, allowed for an unprecedented and comprehensive analysis of the ML and cloud evolution during this time. ASTEX was the first boundary-layer experiment to successfully tackle the logistical complexities of the Lagrangian technique over the ocean for an extended period of time (Albrecht et al. 1995; Bretherton and Pincus 1995).

The structure of the ML is influenced more by vertical mixing than by horizontal mixing. It undergoes strong vertical mixing due to mechanically generated shear or buoyant convection (Stull 1988, p. 12), but its interactions with adjacent columns due to horizontal mixing are weak or negligible. This fact was the impetus for focusing on a single column of air and using the Lagrangian method for studying ML structure. Tracking a single air column negates the effects of horizontal advection, which is difficult to reliably ascertain over the ocean. This removes a major uncertainty in thermodynamic and chemical budgets, and expedites comparisons with ML models and parameterizations (Bretherton and Pincus 1995).

The mean velocity of an air column was determined by tracking a balloon (which advected along with the horizontal flow), either by aircraft-measured winds or from synoptic-scale analyses. This technique provides measurements from a frame of reference which moves with the wind (Lenschow 1986, p. 39). This method is not error-proof, however. A balloon samples air motion solely at the level at which it is floating. Its measurements do not represent the mean motion average over all heights in the ML. Furthermore, synoptic-scale analyses over data-sparse areas of the ocean can result in large wind errors, and lastly, aircraft-measured winds are subject to systematic drifts (Lenschow 1986, p. 41; Bretherton and Pincus 1995).

In order to track a single ML air column, several constant-volume balloons were launched from an oceanic research vessel in half-hour increments at the start of each IOP. Each balloon was ballasted to rise approximately 500-750 meters above sea level (roughly the mid-height of the ML) and was equipped with a GPS receiver that determined the balloon location to within plus or minus ten meters in the horizontal and plus or minus 100 meters in the vertical, every five minutes. The balloon transmitted a history of its position for the previous six hours to the aircraft participating in ASTEX. The balloon’s center of mass was used to determine air column position.

Careful flight planning and coordination between aircraft were required to maintain continuous coverage. On every mission, an aircraft intersected the trajectory and attempted to locate the balloons using its onboard receiver. It then flew a sequence of vertically stacked legs, followed by a sounding, while drifting downstream along the trajectory. A common flight path was to fly L-shaped patterns such as a 60-kilometer crosswind and a 60-kilometer along-wind leg at each level in the stack.

Stacks included a near-surface leg below all clouds, at a height of 30-50 meters during the day and 150 meters at night. One or more legs were usually flown slightly beneath the stratocumulus cloud base (but above the base of any cumulus clouds rising into a stratocumulus layer). Another leg was flown just below the ML capping inversion, in the middle of the stratocumulus cloud layer, if one existed. This was followed by a “porpoising” leg, which oscillated up and down through the inversion. Finally, for completeness, an above-inversion leg was flown (Bretherton and Pincus 1995).

The flight legs were nearly perpendicular to the mean wind in the boundary layer, and were flown so that the aircraft flight tracks advected with the wind. If the mean wind trajectory were subtracted from the horizontal projection of the flight track, the flight legs would be nearly on top of each other. Thus, the measurements taken should have been from the same airmass. Since cumulus clouds usually have a diameter of only a few kilometers, it is almost certain that the aircraft was sampling the same cloud structures on successive legs (Wang and Lenschow 1995).

In a vertically sheared ML, the balloon velocity can differ from the mass-weighted ML mean horizontal velocity and provide a misleading trajectory. However, in the weak shear typical of the MLs experienced during ASTEX, this was only a minor source of error (Bretherton and Pincus 1995). During the first Lagrangian IOP, all of the released balloons eventually ended up in the ocean after a few hours due to precip loading by drizzle (Albrecht et al. 1995). If no balloons could be located, the ML-averaged aircraft wind sounding was used for trajectory determination (Bretherton and Pincus 1995).

The first Lagrangian experiment was conducted in a clean marine airmass (Albrecht et al. 1995). The ML evolved from a shallow, drizzling stratocumulus region into a trade cumulus layer with some overlying stratocumulus and deeper convection in 36 hours. Since winds above the ML were similar to those in the ML, mean vertical motion was inferred from changes in the above-ML profiles of ozone and water vapor following the ML airmass. Mean vertical motion gradually changed from downward to upward during hours 12-36, hastening ML deepening and cloud transition from stratocumulus to cumulus (Bretherton and Pincus 1995).

The second Lagrangian experiment took place in an aerosol-polluted airmass which had advected off the continent of Europe (Albrecht et al. 1995). A 200-millibar-deep ML with cumulus rising into intermittent stratocumulus and strong capping inversions of 6-8 degrees Kelvin were tracked for 36 hours with almost no change in structure.

The two Lagrangian IOPs demonstrated the effectiveness of the Lagrangian strategy for observing the evolution of an ML airmass over a period of up to two days (Bretherton and Pincus 1995). Due to their detail and consistency, the Lagrangian datasets make superb case studies for the processes that regulate marine boundary-layer cloudiness (Bretherton et al. 1995).

C. OBSERVATIONAL PLATFORM

Planning an observational study requires a fundamental understanding of the platforms and instrumentation used. Techniques for gathering, analyzing, and synthesizing data need to be thoroughly understood. A researcher must be cognizant of how measurements are made and the limitations of the instruments in the environment in which they are being used (Lenschow 1986, p.2). A discussion regarding how common atmospheric variables were obtained during ASTEX follows.

1. Aircraft

A Lockheed L-188C aircraft known as the Electra (Figure 6) was used to perform extensive studies of the boundary layer. The National Center for Atmospheric Research (NCAR) modified this aircraft to host a wide variety of instrumentation for atmospheric study (Figure 7; RAF 2000). The major variables obtained from Electra and used in this study are virtual potential temperature, liquid water content, specific humidity of water vapor, three-dimensional wind vectors, altitude, cloud droplet size and concentration, and ozone.

Figure 6. NCAR Electra aircraft (From RAF 2002).

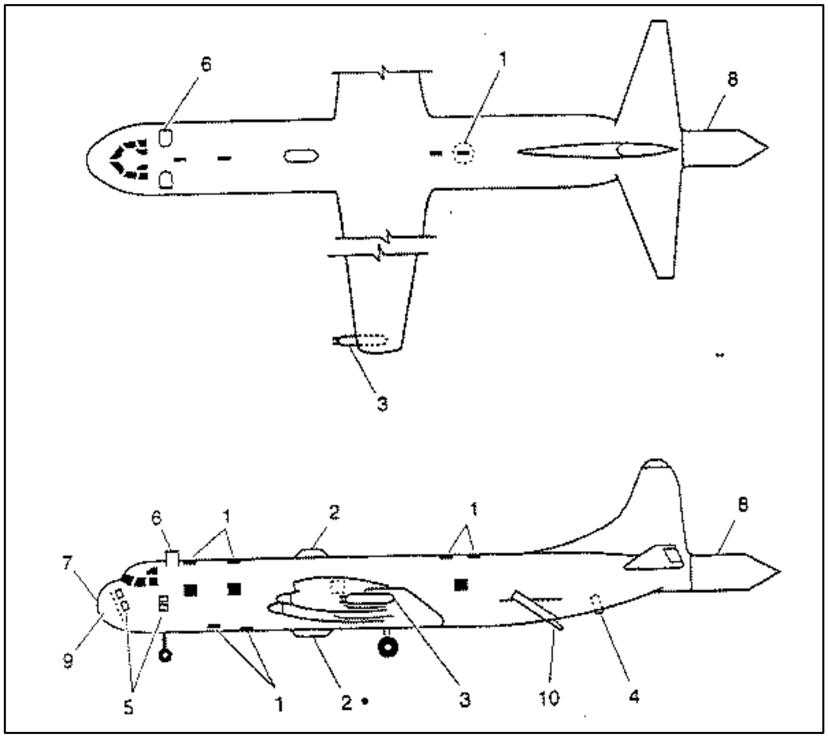

1. **Fuselage Apertures (15)**
2. **Radiometer Pods (2)**
3. **Pylon Wing Boom Probes (2)**
4. **Dropsonde Dispenser**
5. **Sensor Mount Pods (8)**
6. **Sensor Pylons (2)**
7. **Radome Gustprobe**
8. **ELDORA (Doppler Radar)**
9. **Nose Radar**
10. **Oceanographic Probe**

Figure 7. External configuration of the Electra aircraft (After RAF 2002).

2. Instrumentation

Temperature was measured with a Rosemount Type 102 electrical resistance wire thermometer mounted on the forward fuselage of Electra (Ruth 1996). This piece of equipment can calculate temperature with great precision, making the resistance thermometer one of the most accurate instruments available for measuring temperature (Sears et al. 1987, p.343). In addition to being highly accurate, this thermometer was employed because the effect from cloud wetting on its sensors is negligible (McDowell 1999). Sensor wetting can result in cooling, causing a thermometer reading to be a couple of degrees Celsius below the actual atmospheric temperature (Lenschow 1986, p. 52). The output from the Rosemount thermometer was compared with the output from an infrared temperature sensor, and it was determined that wetting of the thermometer's sensors by cloud water was not a problem during ASTEX (Wang and Lenschow 1995). Virtual potential temperature magnitudes were derived from temperature and specific humidity measurements (McDowell 1999).

Specific humidity was measured with an NCAR-developed Lyman-alpha hygrometer, using a General Eastern Model 1011B dewpoint hygrometer as an absolute reference. The Lyman-alpha hygrometer was designed to provide fast-response, high-resolution measurements. This instrument is highly accurate, with one notable exception--it is susceptible to sensor wetting. Therefore, measurements taken inside clouds are highly suspect and represent the basic limitation of this piece of equipment (Wang and Lenschow 1995; RAF 2000). A CSIRO (Commonwealth Scientific and Industrial Research Organization) total water sensor was utilized within clouds.

It is much slower than the Lyman-alpha hygrometer, but its value lies in its reliability. It is not prone to sensor wetting. Thus, it can be used in or out of clouds (Wang and Lenschow 1995). This sensor was also used to assess liquid water content.

Wind direction and speed calculations are challenging to obtain aboard aircraft. They are not straightforward measurements because of their relative motion with respect to the earth and the aircraft. The velocity of the air with respect to the earth, $\mathbf{V}$, is obtained by adding the velocity of the aircraft with respect to the earth, $\mathbf{V}_\mathbf{p}$, and the velocity of the air with respect to the aircraft, $\mathbf{V}_\mathbf{a}$:

$$\mathbf{V} = \mathbf{V}_\mathbf{p} + \mathbf{V}_\mathbf{a} \text{ (Lenschow 1986, p. 39).}$$

Airplane motion was computed by an inertial navigation system (INS) in conjunction with GPS data. The components of $\mathbf{V}_\mathbf{a}$ were computed from a differential-pressure gust probe system (Figure 8) located on the radome of the Electra’s nose section. Airflow measurements were recorded from an aircraft frame of reference, so these measurements were first converted to an earth-based reference by using the three airplane attitude angles (i.e., yaw, pitch, and roll) measured by the INS. These values were then subtracted from the airplane velocity components, which were obtained from integrated accelerometer outputs (corrected for Coriolis accelerations) in an earth-based frame of reference.

There are additional complexities to consider with aircraft motion. As the aircraft moves along, it severely distorts the flow field. It also compresses the air in front of it, which leads to adiabatic heating. Corrections and calibration techniques must be employed to remove these unwanted factors (Jonsson 2004, personal communication).

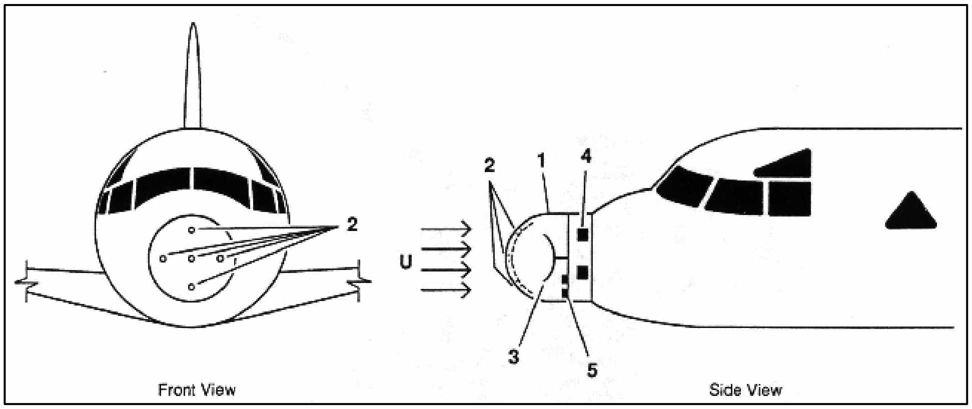

1.	**Instrumented Radome**	**2.**	**Differential Pressure Ports**
3.	**Nose Weather Radar**	**4.**	**Sensor Mount Pads**
5.	**Pressure Transducers**		

Figure 8. Differential-pressure gust probe system (After RAF 2001).

The gust probe system on Electra had a resolution of 0.012 m s^{-1} and an accuracy of plus or minus 0.1 m s^{-1}. Thus, even though air motion calculations can be complex and even cumbersome, they are nonetheless obtainable and highly precise. Electra’s radome was heated and contained a device for trapping ingested water (RAF 2001); thus, it was used both in and out of clouds (RAF 2002).

Radio and radar altimetry were used to calculate Electra’s geometric height above the surface. Altimeters determine altitude by measuring the time it takes an electromagnetic signal to travel from a transmitter to the underlying surface and back to the receiver (Glickman 2000, p. 33). A Collins ALT-55 radio altimeter was employed to obtain heights below 780 meters, while a Stewart Warner APN-159 radar altimeter was used to measure altitudes between 500 and 10,000 meters. Both altimeters are highly accurate with a resolution of one-tenth of a meter (RAF 2002).

Liquid water content, cloud droplet size, and cloud droplet concentration (the number of droplets per cubic centimeter) were measured with a Particle Measurements Systems, Inc. Forward Scattering Spectrometer Probe (FSSP). The FSSP-100 Cloud Probe (Figure 9) is part of a general class of instruments known as optical particle counters. Inside the FSSP-100, a hybrid laser beam comprised of helium and neon is focused at the center of an inlet that faces into the oncoming airstream. Liquid water content and cloud droplet size and concentration were determined by the droplets' scattering effect on the laser beam (RAF 1989).

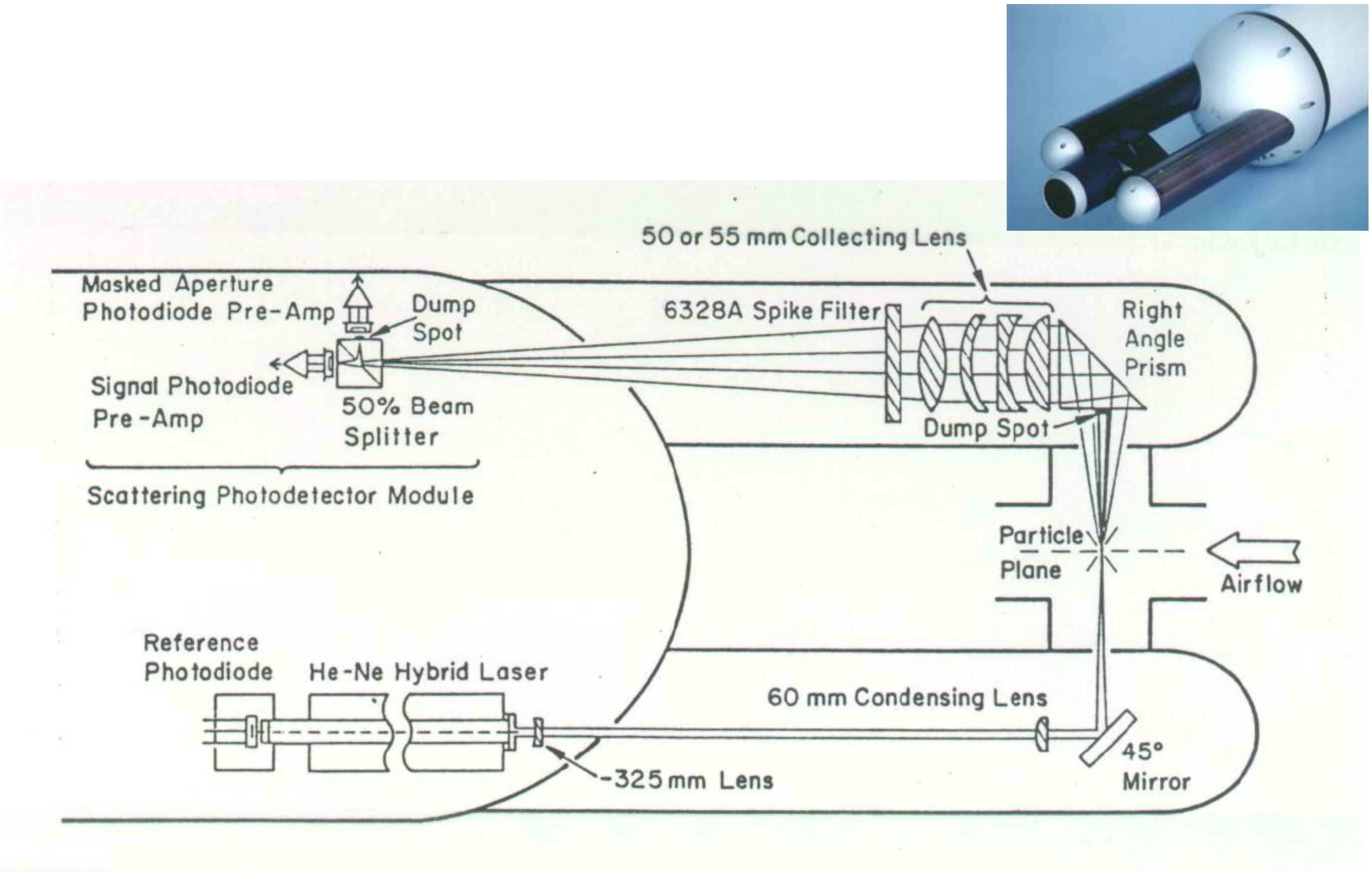

Figure 9. Picture and schematic of the FSSP-100 Cloud Probe (From RAF 1989).

Tropospheric ozone was measured as a tracer. Ozone measurements aided in the analysis of entrainment zone structure at the top of the planetary boundary layer. Ozone measurements were used to determine the ozone cloud-top jump conditions across the entrainment zone (McDowell 1999).

A nitric oxide chemiluminescence ozone sensor developed by NCAR was used to make the ozone measurements (Wang and Lenschow 1995). Nitric oxide (NO) can interconvert with nitrogen dioxide (NO_2) relatively easy in the atmosphere, resulting in catalytic cycles leading to ozone formation in the troposphere:

$$NO_2 + O_2 \rightarrow NO + O_3$$

(Ahrens 1994, p. 455; Glickman 2000, p. 526).

When these molecules interact, a chemiluminescent reaction occurs and this light can be measured. The amount of light detected is proportional to the amount of ozone present (Gregory et al. 1987).

Instrument redundancy was the norm aboard Electra. A single temperature sensor was not solely relied upon, for example. There were several temperature sensors on the aircraft. This allowed output from different sensors to be compared, and it eliminated reliance on a solitary piece of equipment. The onboard computer system could display data in either real-time or post-processing modes. One data system display station was located in the cockpit for the benefit of the flight crew and the mission scientist. Four additional display stations were located in the main cabin of the aircraft. Video cameras were mounted in the cockpit and on the side of the aircraft, which could be viewed in real-time on any of the display stations.

Data was processed and quality controlled by NCAR’s Research Aviation Facility (RAF) Project and Data Support Group (RAF 2002). They produced output files for both measured and derived variables. All of the data sets used in this study consist of 20 samples per second, with the exception of the CSIRO water sensor and the dewpoint hygrometer, which were only available at a rate of one sample per second (Wang and Lenschow 1995). Lastly, a quick-look, post-flight data-processing system was onboard to provide further quality assurance (RAF 2002).

THIS PAGE INTENTIONALLY LEFT BLANK

III. DATA ANALYSES AND RESULTS

A. AIRCRAFT FLIGHT INFORMATION

An analysis of the information obtained during ASTEX began with data collection from NCAR's Research Aviation Facility. Using the retrieved data, a MATLAB program was created to display Electra's flight tracks as a set of simple line plots (see Figure 10).

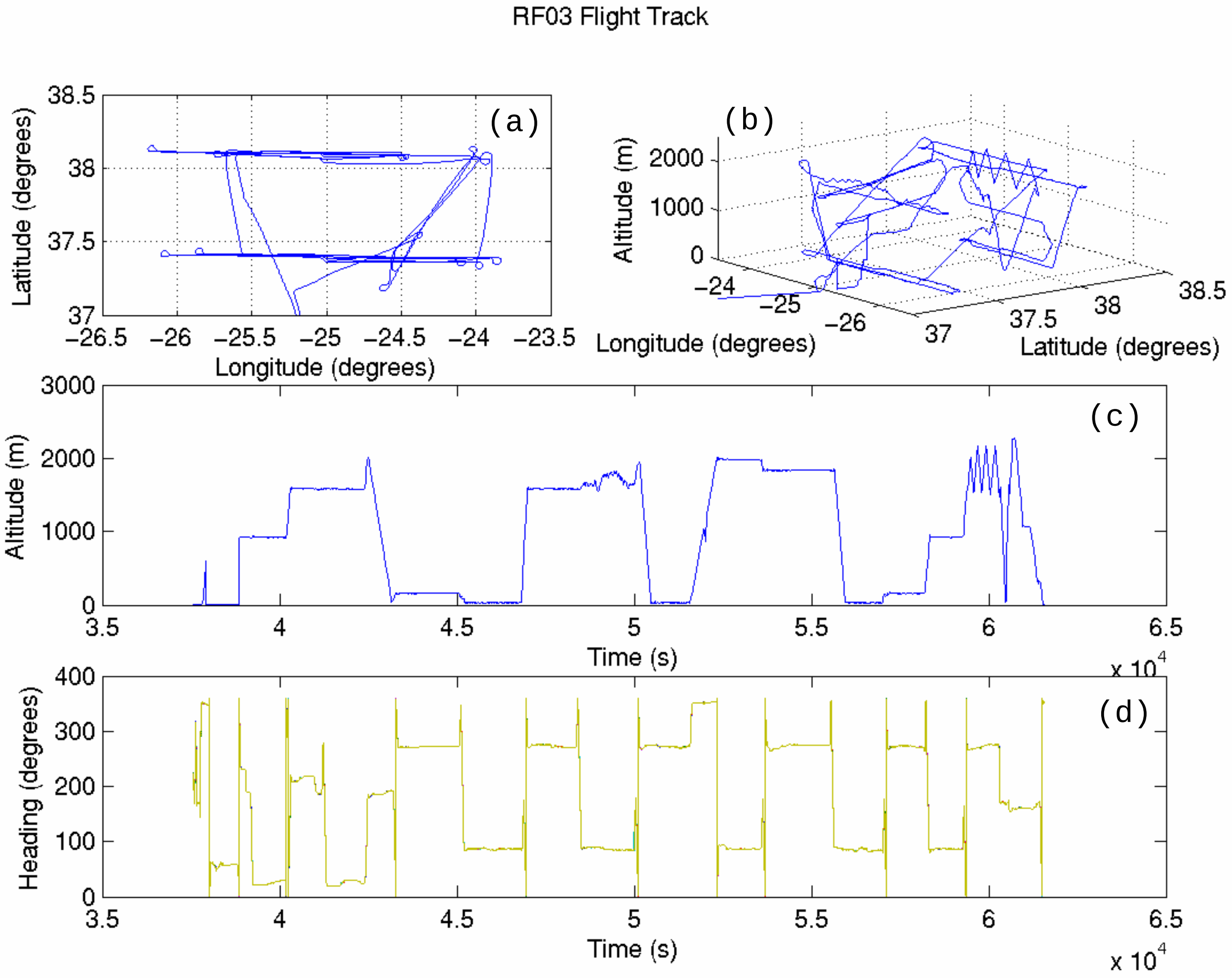

Figure 10. A graphical representation of Research Flight 3. (a) Latitude/Longitude. (b) Latitude/Longitude with respect to altitude. (c) Vertical motion and altitude with respect to time. (d) Heading with respect to time.

Flight tracks were created for all 17 of Electra’s flights. These flight tracks provided information about Electra’s latitude and longitude, altitude, vertical motion, and heading. An examination of Electra’s “porpoising” legs (see Figure 11) offered an initial indication of entrainment-zone characteristics. The pattern of these flight legs is the result of the aircraft flying up and down through the cloud top. Electra’s pilot was instructed to fly in this manner so that air samples could be obtained above, below, and within the cloud layer.

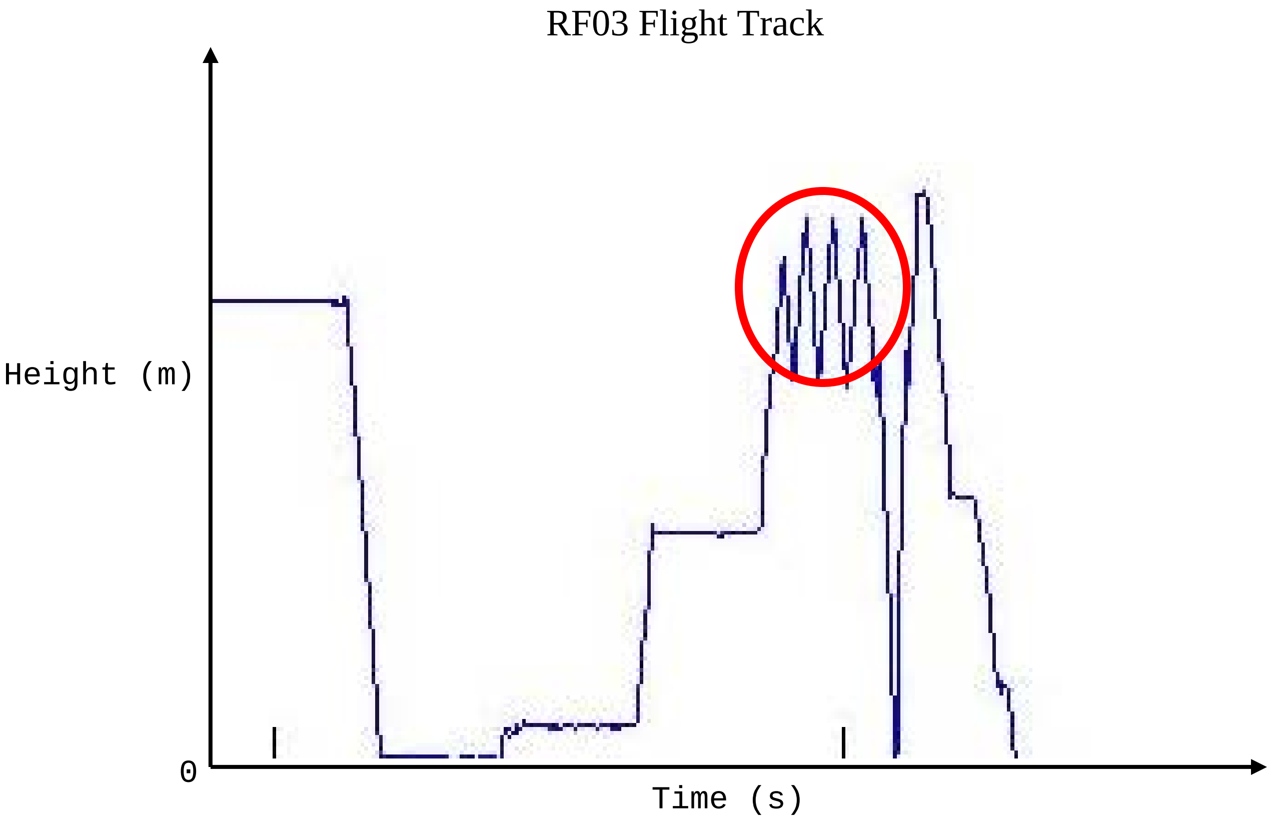

Figure 11. Zoomed-in segment of Research Flight 3’s flight track. The “porpoising” legs (encircled in red) oscillate up and down through the cloud layer.

B. GENERAL BOUNDARY-LAYER CHARACTERISTICS

1. Vertical Variations of Cloud and Turbulence

The individual flight legs from each flight track were examined to determine entrainment-zone structure. From this examination, vertical profiles of several atmospheric variables were created. Figure 12 shows an example of the sounding profiles generated. These soundings were made on June 4, 1992 during the first Research Flight (RF01) of ASTEX.

Cloud liquid water content and microphysical properties are shown in Figures 12a, 12h, and 12k for liquid water content, cloud droplet number concentration, and mean droplet diameter size, respectively. The measurements show a relatively thin cloud layer relative to a much deeper boundary layer. For liquid water content (Figure 12a), the measurements from the CSIRO water sensor (blue line) and the FSSP-100 Cloud Probe (red) are shown. The CSIRO sensor consistently underestimated the cloud water content in comparison with the data integrated from the FSSP-100 droplet spectrum; however, both sensors yielded the same general information. The thermodynamic structure of the boundary layer is easily seen in the profiles of Figures 12b, 12c, and 12d, where decoupling is evident in the temperature, water vapor, and ozone soundings. The three components of the mean wind can be seen in Figures 12e - 12g. Turbulence can be inferred from these soundings by the amount of variation in the wind speed.

Figures 12i, 12j, 12l, 12m, and 12n show the vertical variations of the perturbation field for virtual potential temperature (θ_v), water vapor specific humidity (q_v), and the u, v, and w components of the wind. These perturbations were obtained using wavelet filtering to remove large-scale variations (e.g., the meandering of vertical velocities which were not realistic). The plots of the filtered perturbations allow for easier visualization of turbulence strength. It should be kept in mind, however, with strong vertical gradients some erroneous perturbations may result from the filtering process, as seen at the cloud top in Figures 12i and 12j. Thus, these perturbations should be viewed together with the unfiltered field shown in the upper panels of the same column in Figure 12.

The perturbation velocity fields show strong turbulence up to about 626 m above the surface. Above this height, the turbulence field is patchier. Examinations of the θ_v and q_v profiles reveal a sharp increase in θ_v and a corresponding decrease in q_v at 626 m, indicating that the boundary layer is decoupled at this altitude. The θ_v and q_v perturbation fields (Figures 12i and 12j) also show a decrease in intensity between the surface-based mixed layer and the cloud-mixed layer above. The large magnitudes of the θ_v and q_v perturbations at the cloud top are related to the filtering limitations of sharp gradients as discussed earlier.

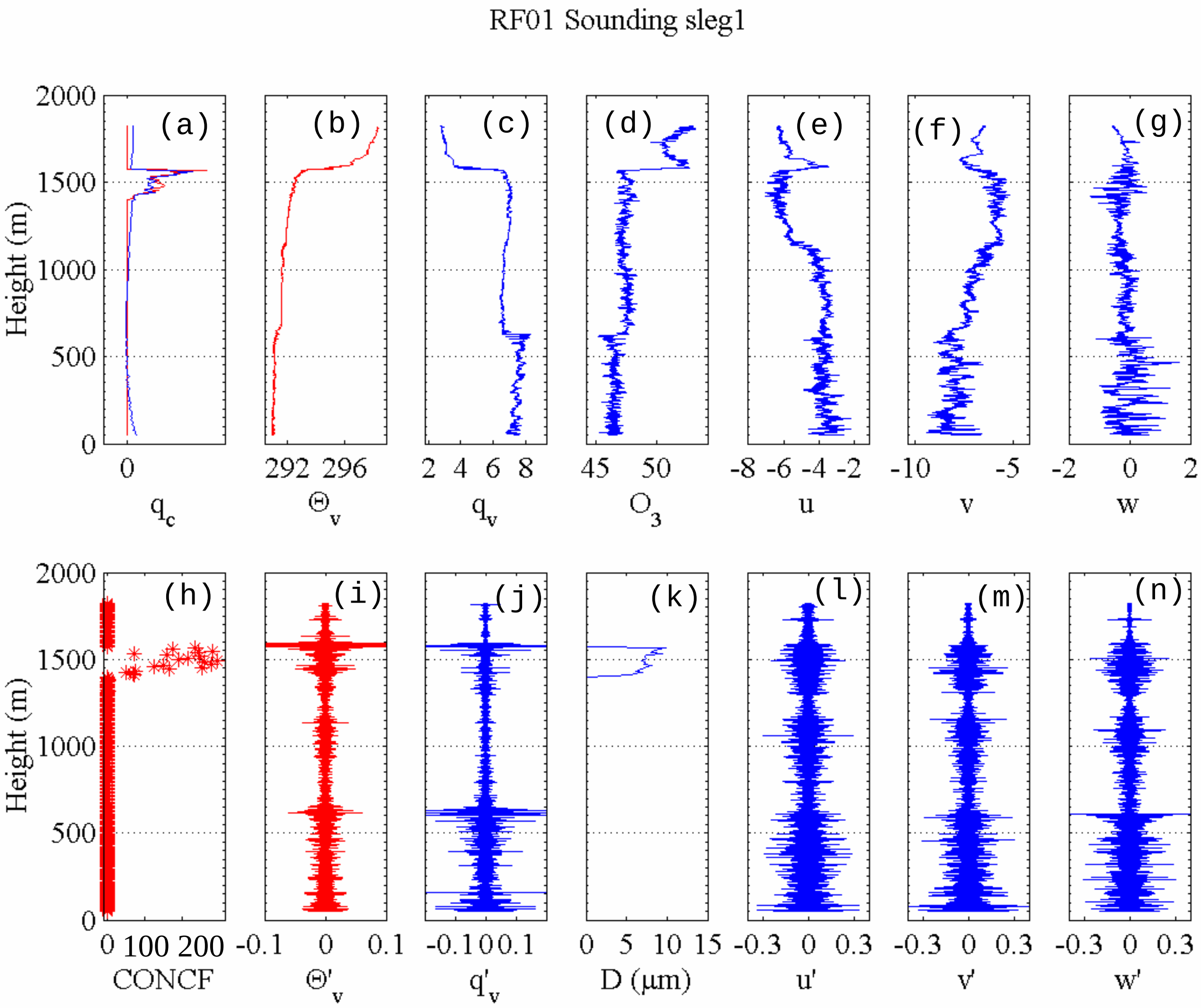

Figure 12. Vertical profiles from Research Flight 1, leg 1. (a) liquid water content (g kg^{-1}), (b) virtual potential temperature (K), (c) specific humidity of water vapor (g kg^{-1}), (d) ozone (ppbv), (e) u wind speed component (m s^{-1}), (f) v wind speed component (m s^{-1}), (g) w wind speed component (m s^{-1}), (h) cloud droplet concentration (N cm^{-3}), (i) θ_v perturbations, (j) q_v perturbations, (k) droplet size (µm) (l) u perturbations, (m) v perturbations, (n) w perturbations.

2. The Entrainment Zone

The soundings shown in Figure 12 depict a classical view of cloud-topped boundary layers. A sharp temperature inversion occurs immediately above the cloud top, accompanied by a sharp decrease in water vapor. Strong gradients in ozone and the mean wind are also seen. Due to the numerous porpoising legs flown during the many flights of ASTEX, a large amount of ascending and descending soundings were constructed through the interface at the cloud top. This allowed for an in-depth examination of the fine-scale structure of the cloud top from a large number of samples. An analysis of these soundings provided a comprehensive understanding of the physical processes involved in the entrainment zone.

Soundings from Research Flight 6 (Figure 13) contain examples of atypical (from the standpoint of the classical view) vertical profiles for cloud-topped boundary layers. Another example of soundings deviating from the classical model is shown in Figure 14. During ASTEX, soundings like the ones shown in these two figures were common. Thus, rather than being the exception, soundings which did not match the classical viewpoint were the norm.

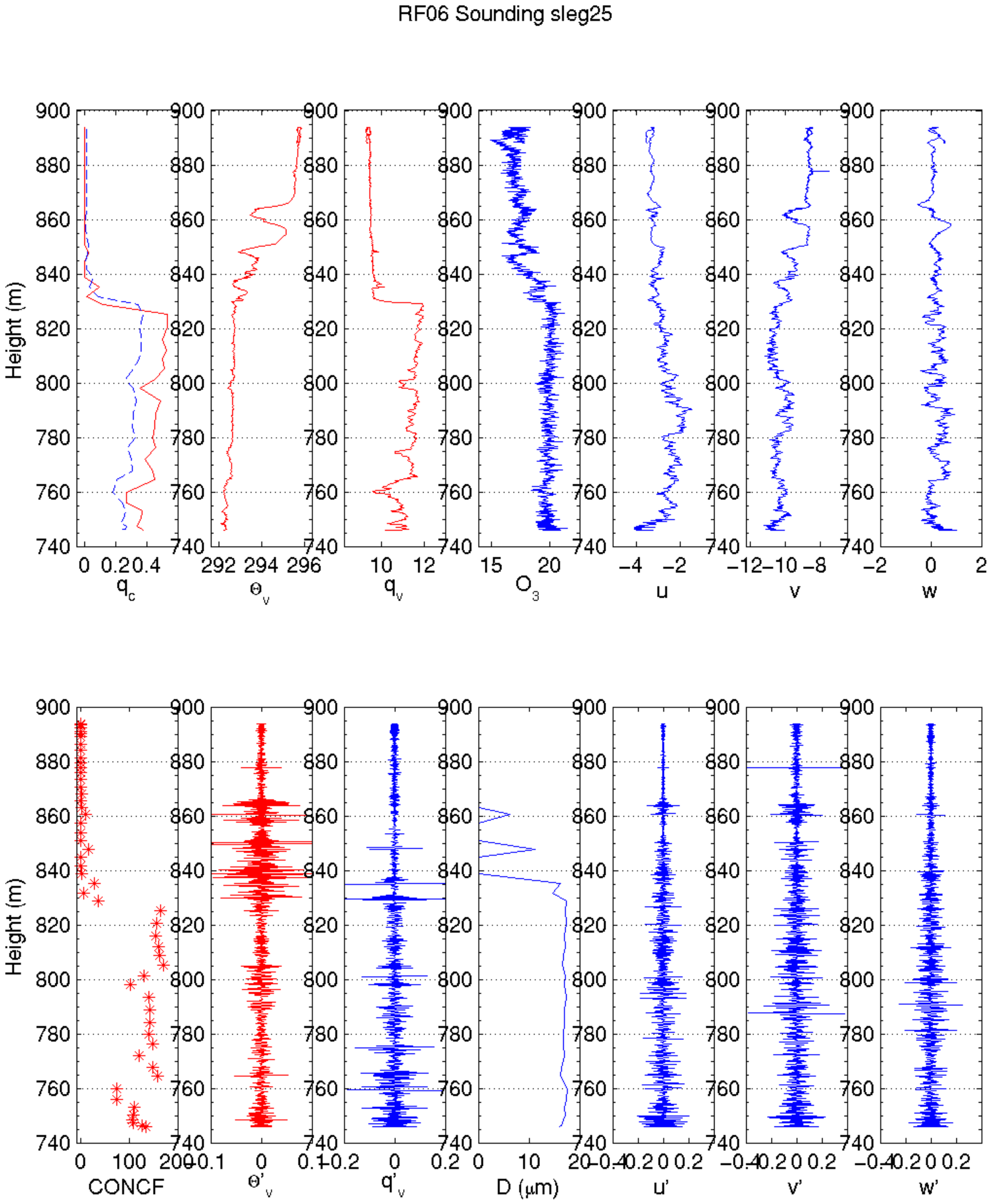

Figure 13. Same as in Figure 12, except for Research Flight 6, leg 25.

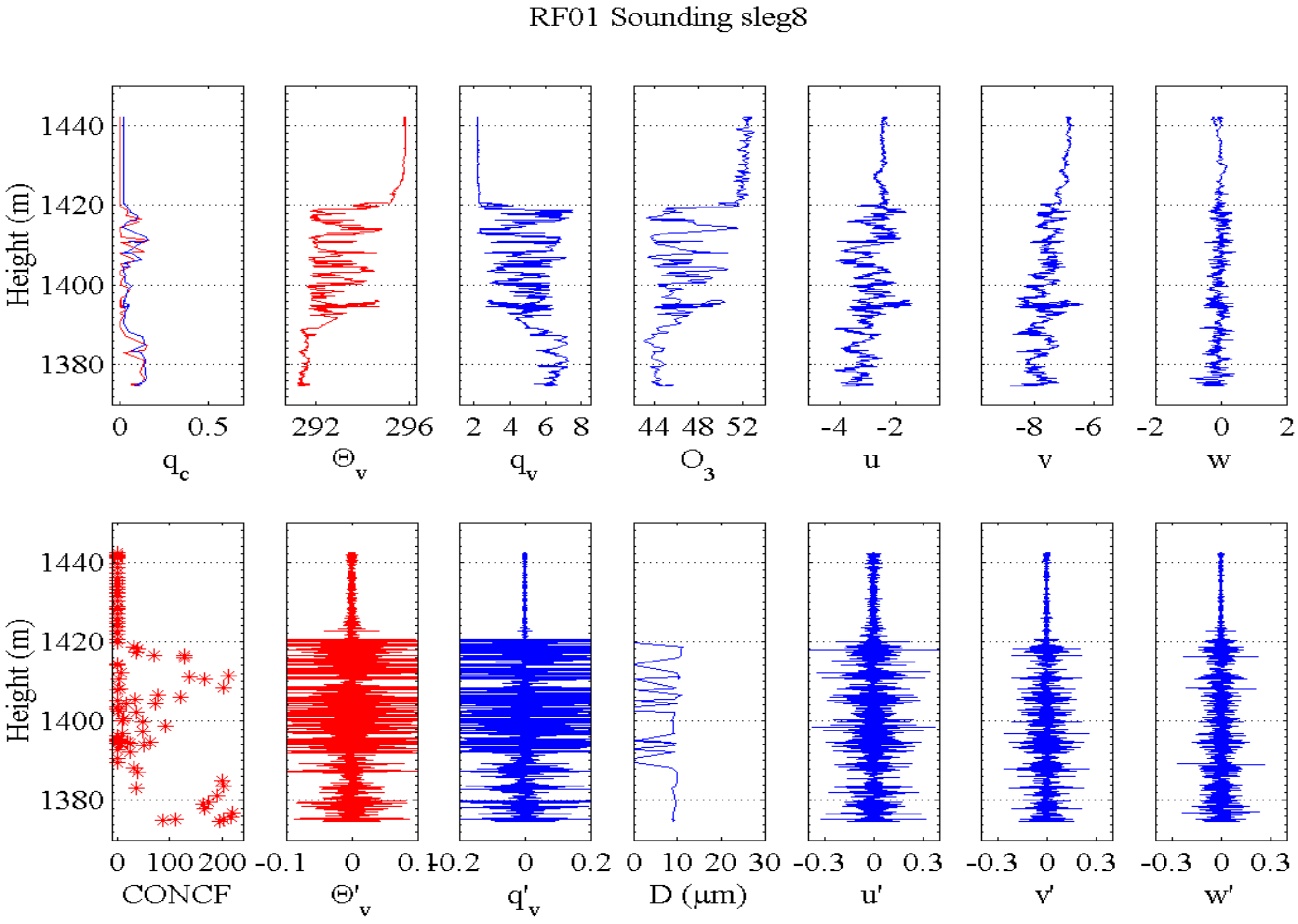

Figure 14. Same as in Figure 12, except for leg 8 of Research Flight 1.

In Figure 14, strong vertical variations can be seen in temperature, water vapor, and ozone in a layer between 1389 and 1419 m, where the cloud liquid water content is reduced from the solid-cloud layer below. These soundings clearly show boundary-layer air parcels above the cloud-mixed layer intermingling with air parcels that resemble free-atmosphere air. Autonomous pockets of the two different airmasses indicate uneven or inhomogeneous mixing between the free atmosphere and the boundary layer. Consequently, this area of transition is defined as the entrainment zone in this thesis.

The sharpest temperature inversion in Figure 14 is located at the top of the wispy cloud region, where low liquid water amounts are indicated. The steepest gradients in water vapor and ozone are also found here. However, a new inversion and a gradient layer for water vapor and ozone appear to be developing immediately above the solid-cloud top at 1392 m.

The height of the solid-cloud top as seen from liquid water content and droplet concentration measurements is at 1387 m. This top is consistent with the sharp gradients observed in water vapor and ozone. However, the sharpest temperature inversion is found 32 m higher, at an altitude of 1419 m. Strong turbulence signatures extend to the base of this sharp inversion.

From the soundings in Figures 13 and 14, entrainment zones can be identified where mixtures of boundary-layer and free-atmosphere air exist within a thin layer tens of meters above the solid-cloud top. Liquid water profiles show protrusions of cloudy air within the entrainment zones.

Turbulence in both entrainment zones varies from none to the same level as within the boundary layer.

C. ENTRAINMENT-ZONE STRUCTURE FROM THE LAGRANGIAN IOP I FLIGHTS

The remainder of this thesis focuses on my second major objective: How does the entrainment process at the cloud top impact cloud evolution in the boundary layer? Stull (1988, p. 575) indicates that entrainment and air parcel motion are nonlocal processes that are best described using Lagrangian approaches. To this end, aircraft soundings from the three Lagrangian IOP I flights (RF05, RF06, and RF07) are focused on from this point forward. Numerous soundings were made in different cross-sectional measurements through the local cloud top during these flights. Because of progressively increasing SSTs with each flight, the Lagrangian IOP I measurements also represent cloudy boundary layers under different large-scale forcings. Hence, the relationship between the properties of the entrainment zone and large-scale forcing can be examined.

1. Boundary-layer Composition

Lagrangian IOP I was conducted between the 12th and 13th of June, 1992. Figure 15 illustrates the flight track and SST of each of the individual flights. The general location of the three flights represents a downwind trajectory following the Lagrangian measurement strategy and the movement of the constant-pressure balloons (Albrecht et al. 1995). Table 1 lists the latitude and the SST of each flight. Measurements from the three flights have been studied previously (Albrecht et al. 1995; Bretherton and Pincus 1995) with a focus on cloud and boundary-layer evolution. Figure 16 (from Albrecht et al. 1995) depicts the cloud evolution seen from these three flights. To further explain the cloud development seen in Figure 16, Figures 17 through 20 are used to illustrate the vertical structure of the boundary layer and the cloud layer for each flight.

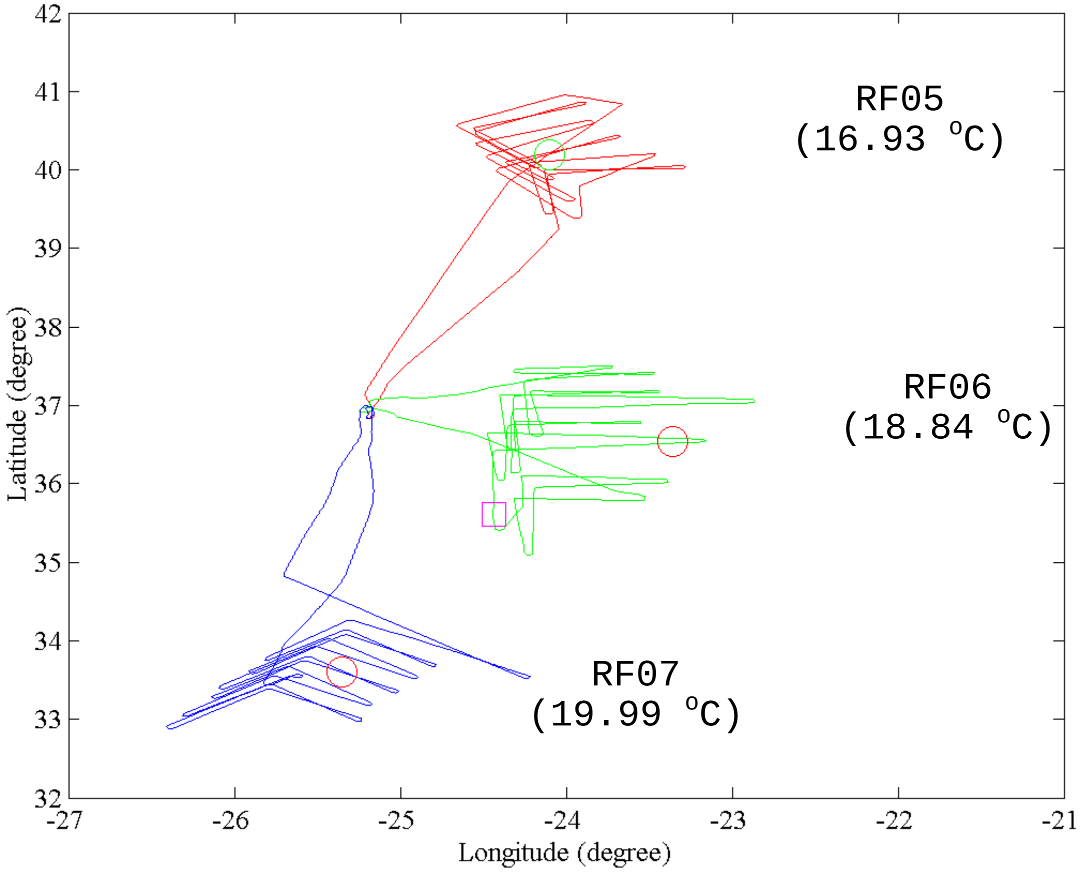

Figure 15. Flight tracks and sea surface temperatures of the three flights during Lagrangian IOP I. RF06 is approximately 410 km south of RF05, and RF07 is about 350 km south-south-west of RF06. The circles and the square denote the location of soundings discussed in a later section.

Table 1. Latitude and sea surface temperature of the Lagrangian IOP I flights.

Flight	Latitude	Sea Surface Temperature
RF05	40° N	17° C
RF06	37° N	19° C
RF07	34° N	20° C

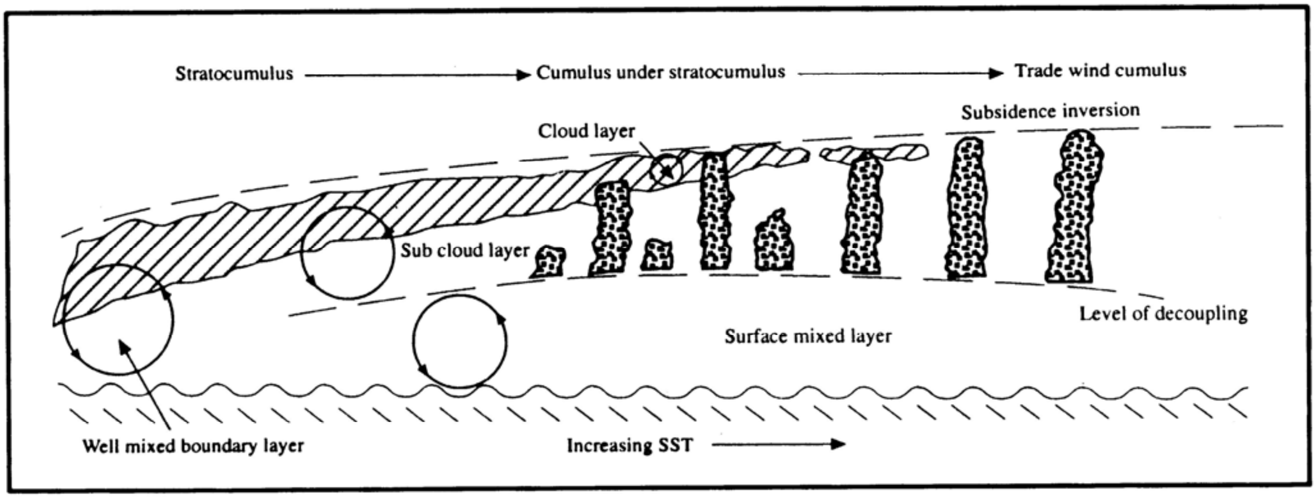

Figure 16. A diagram illustrating the transition from stratocumulus to trade wind cumulus during ASTEX (From Albrecht et al. 1995).

The first flight of Lagrangian IOP I occurred over the coolest water of all three flights. The deep sounding shown in Figure 17 indicates a boundary-layer height of 571 m, as evidenced by the vertical extent of the well-mixed layer and the solid-cloud top. The wind field, specific humidity, and liquid water profiles all indicate an abrupt change immediately at the cloud top. However, the temperature inversion above the cloud top is inconsistent with the data represented by the other soundings. The weak temperature inversion may indicate a problem with the wire thermometer's output in this case. On a final note, the liquid water sounding has an adiabatic profile. This feature is more evident in the soundings from RF05 versus the soundings from RF06 and RF07.

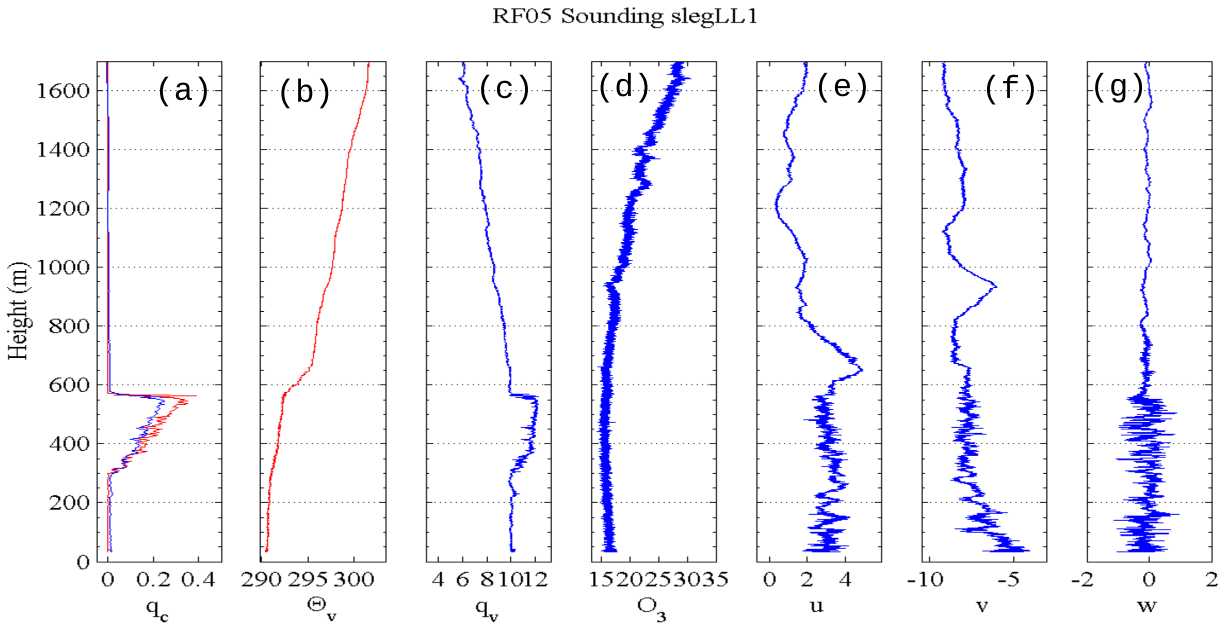

Figure 17. Vertical profiles from Research Flight RF05 on 12 Jun 92 at 2140 UTC. (a) liquid water content (g kg^{-1}), (b) virtual potential temperature (K), (c) specific humidity of water vapor (g kg^{-1}), (d) ozone (ppbv), (e) u wind speed component (m s^{-1}), (f) v wind speed component (m s^{-1}), (g) w wind speed component (m s^{-1}). The location of these soundings is shown as a red circle on the flight track of RF05 (Figure 15).

Research Flight 6 was flown over a lower latitude/greater sea surface temperature than Research Flight 5. Significant variations of the cloud and the boundary layer were observed. According to Albrecht et al. (1995; Figure 16), the measurements of RF06 were made in the transitional region where the cloud layer was thinner and more discontinuous. Figure 18 (RF06) shows soundings from a region where the boundary layer is relatively shallow, but deeper than the boundary layer seen in Figure 17 (RF05). The lower half of the cloud layer appears to be adiabatic in nature (with respect to liquid water content); however, the upper half of the cloud layer deviates from a linear adiabatic profile. This suggests that cloud-top mixing and entrainment are more prevalent in boundary layers with higher SSTs.

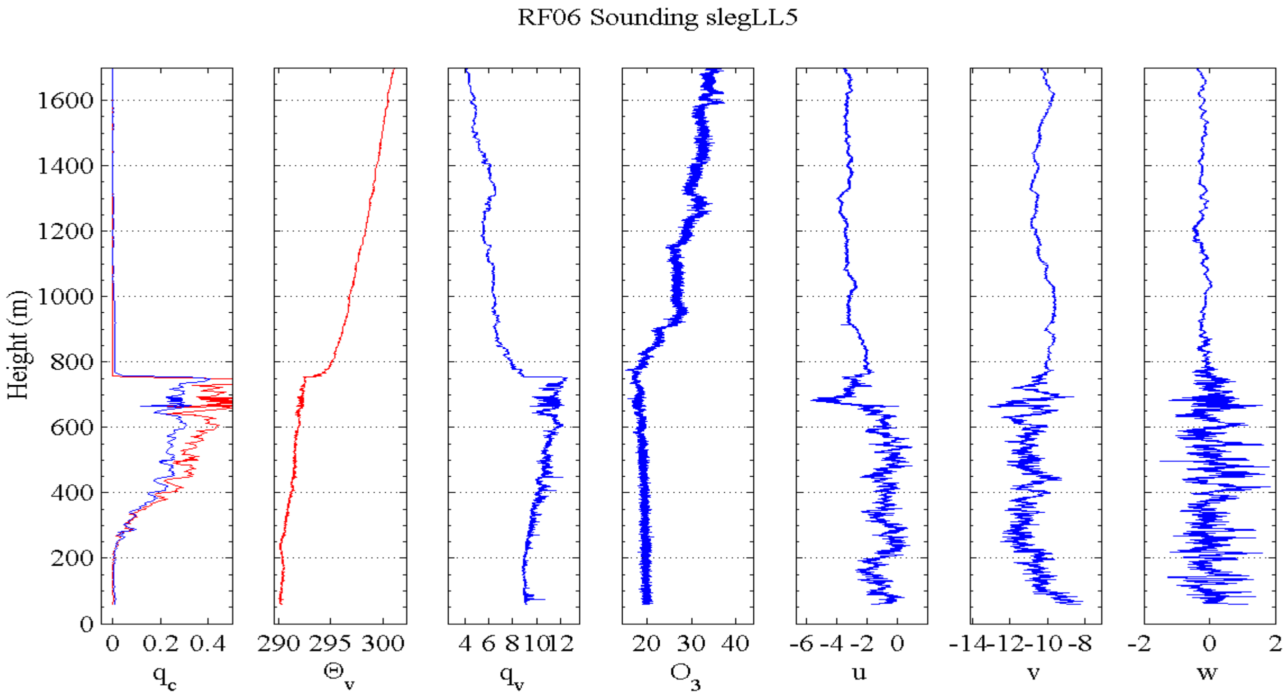

Figure 18. Same as in Figure 17, except for RF06 on 13 Jun 92 at 0820 UTC. The location of this sounding is represented by a red circle on the flight track of RF06 (Figure 15).

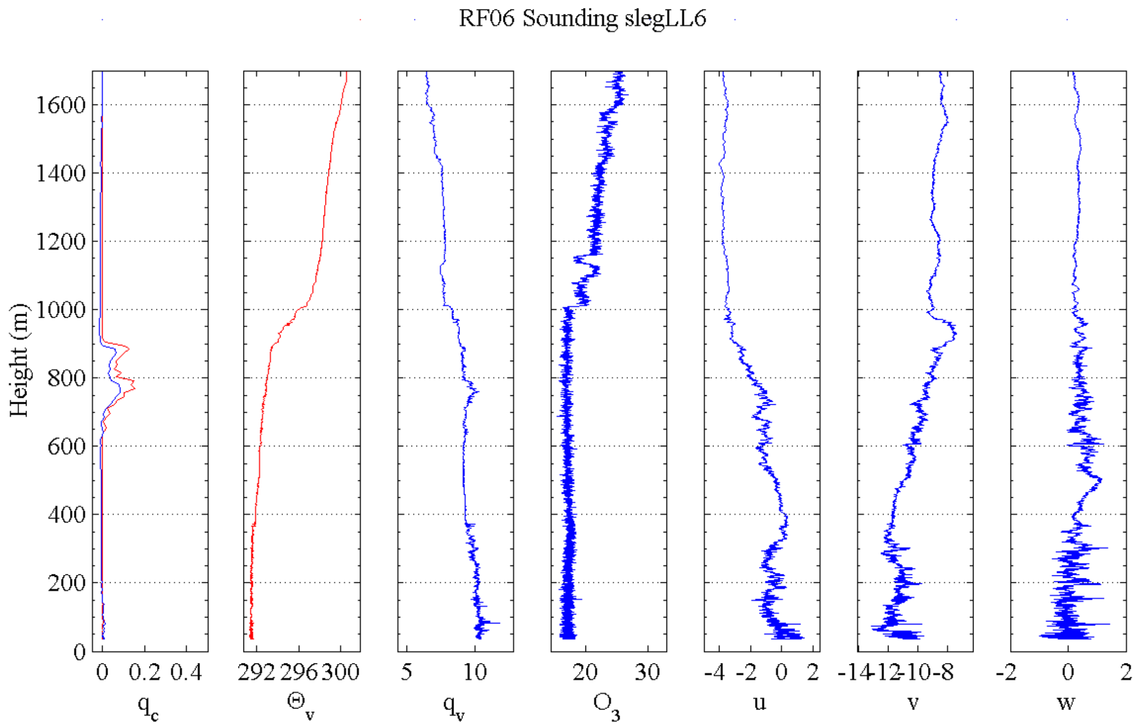

Figure 19. Same as in Figure 17, except for 13 Jun 92 at 0850 UTC (RF06). The location of this sounding is shown as a magenta square on Figure 15.

Figure 19 depicts cloud and boundary-layer structure during Research Flight 6 approximately 140 km downstream from the soundings seen in Figure 18. Here, the boundary layer is deeper (about 900 m) and the cloud layer is thinner, as evidenced by very little liquid water amounts. The boundary layer is clearly decoupled at about 390 m, where a small temperature and water-vapor jump can be identified. Furthermore, turbulence significantly decreases above this height. At the cloud top, the temperature inversion is much weaker and deeper with weak turbulence extending to approximately 1000 m. Above this height, ozone values start to significantly differ, and in accordance with the temperature and water vapor measurements, appear to have the characteristics of free-atmosphere air. These soundings indicate that the cloud deck is too thin to generate sufficient cloud-top radiative cooling (which would lead to stronger turbulence signatures in the upper boundary layer), and that the previous cloud top was at about 1000 m.

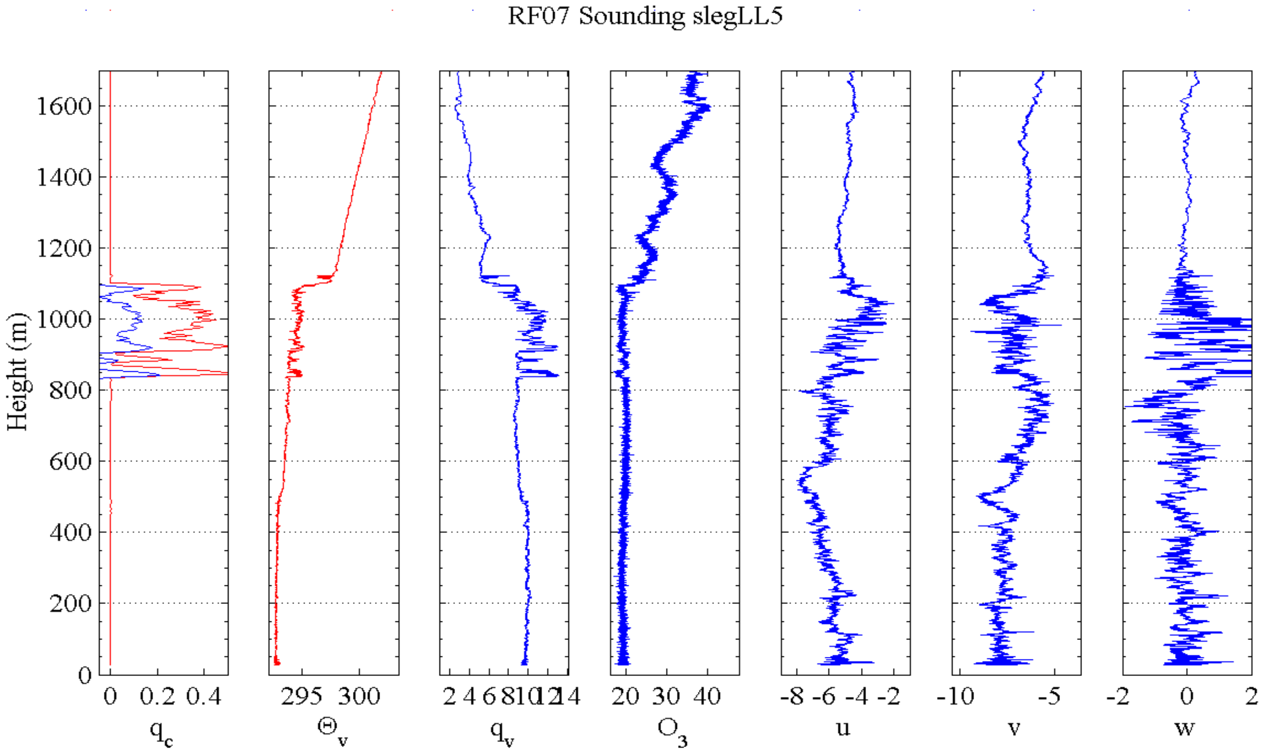

Figure 20. Same as in Figure 17, except for 13 Jun 92 at 2120 UTC (RF07). The location of this sounding is shown as a red circle on the flight track of RF07 (Figure 15).

Research Flight 7 was flown over the greatest sea surface temperature/lowest latitude of all IOP I flights (Figure 15). Here, the solid-cloud top (the extent of the mixed layer) increased to about 1080 m (Figure 20). Unlike the second sounding from RF06 (Figure 19), the cloud layer on this sounding is thicker and radiatively active, resulting in a sharp inversion and a sharp decrease in water vapor immediately above the cloud top. Decoupling of the boundary layer is evident at about 490 m above sea level.

It can be seen from the four soundings along the trade-wind trajectory that boundary-layer height increases as an air column moves over progressively warmer water as depicted in Figure 15. The cloud deck appeared to be solid up through the early part of RF06, and became more variable and wispy afterwards (later part of RF06 and RF07). Lastly, the boundary layer consistently decouples over warmer water.

2. Cloud-top Variations

The multiple penetrations through the cloud top from the porpoising or zigzag legs provided a vertical cross section of cloud and boundary-layer properties. This allowed for a spatially coherent view of the cloud top. An example of the cloud-top structure obtained from these sounding legs is given in Figure 21. This type of imagery has not appeared in previous literature for cloud-topped boundary layers.

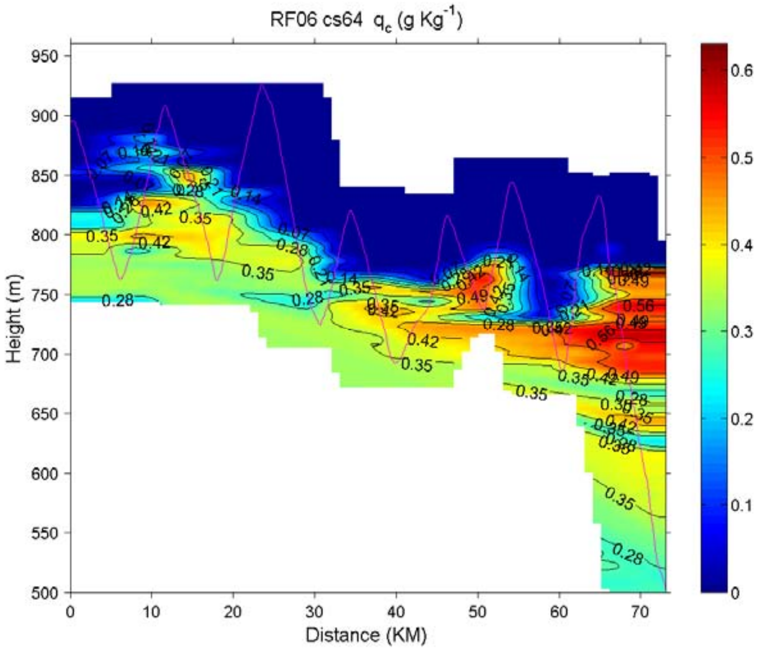

Figure 21. Vertical cross section of liquid water content from one of the zigzag soundings during Research Flight 6 of ASTEX. The measurements from the FSSP-100 Cloud Probe were used in this plot. The thin magenta line denotes the flight track. The horizontal axis represents the distance from the starting point of the flight leg.

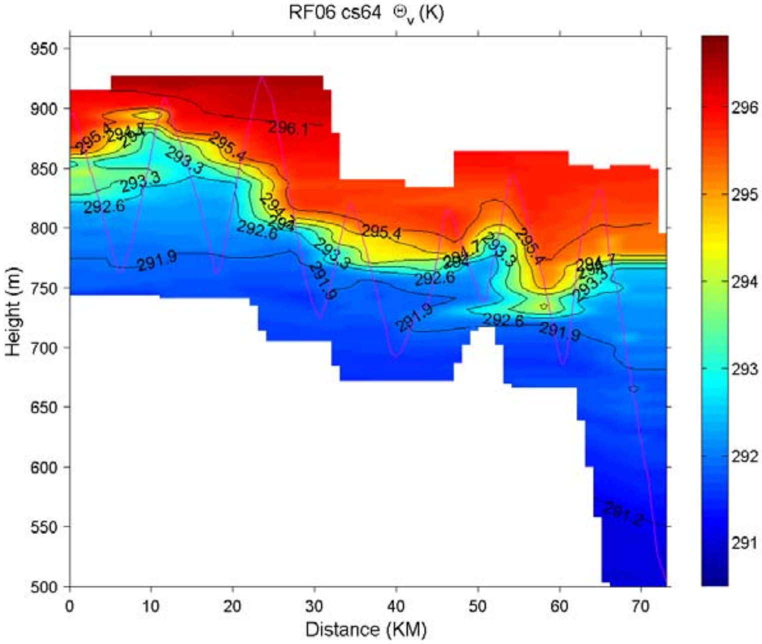

Figure 22. Same as in Figure 21, except for virtual potential temperature.

Figure 22 shows the corresponding variations of the virtual potential temperature field for the same period as Figure 21. The boundary layer (depicted in blue) and the free atmosphere (depicted in red) are clearly separated by a sharp temperature gradient.

Figure 23 depicts the cloud-top structure from Research Flight 5. The dominant feature of the cloud top is an undulating surface which oscillates as a series of troughs and ridges. A noticeable change is evident in the temperature gradient of the cloud-top ridges and valleys. A tight gradient appears to exist in the ridges, while a more relaxed gradient is present in troughs. This fine-scale structure at the cloud top has not been discussed in previous literature, and further statistical analysis is needed to confirm these findings.

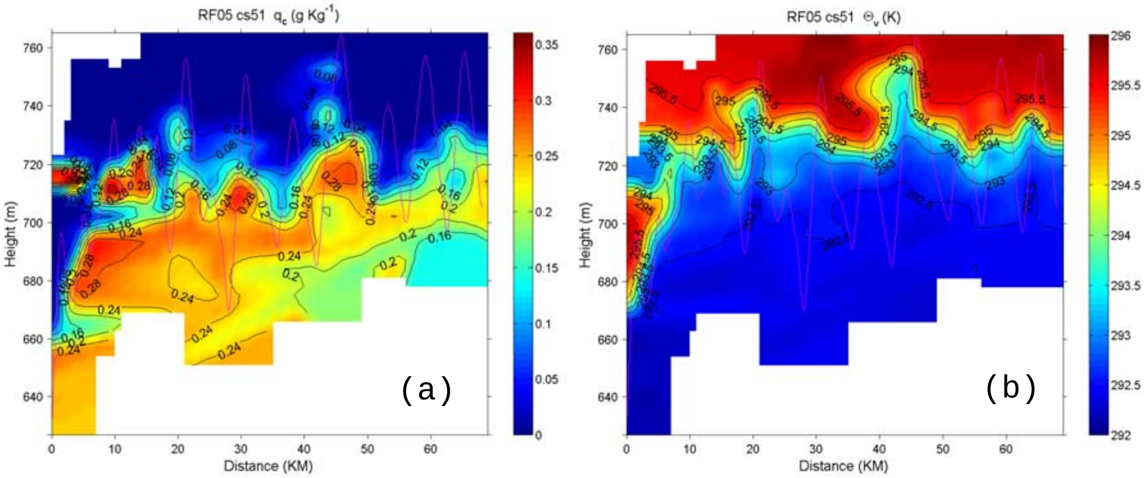

Figure 23. Vertical cross-section of (a) liquid water content (g kg^{-1}) and (b) virtual potential temperature (K) from RF05. The flight track is shown as the thin magenta line. The horizontal axis is the distance from the starting point of the leg.

The depths of the cloud-top ridges and troughs are on the order of 10 to 20 m. The width of these same features is on the order of 5 to 10 km. At 20 km and 45 km into the measurements, small liquid water amounts are present above the ridges of the solid-cloud top. These areas were subsequently defined as regions of wispy cloud matter, and they extended 20 to 30 m above the local solid-cloud top. The air immediately above the solid cloud-top troughs contains little to no detectable remains of cloud droplets.

On the left-hand side of Figure 23a, the cloud layer shown between 710 and 720 m is an artifact of the interpolation scheme used in the plotting routine, as there were no measurements at that level. The separation of the cloud patch from the lower cloud deck at about 10 km into the flight is also the likely result of the interpolation scheme as this too is a data-void region.

Figure 23b shows the horizontal and vertical variations of virtual potential temperature relative to the cloud top. Here, the greatest gradient in temperature is found at the wispy cloud top, and not at the solid-cloud top, although there is a gradual increase in temperature within the wispy cloud region above. If the boundary-layer height were defined by using virtual potential temperature, then the region colored in dark blue would represent boundary-layer air. From an examination of multiple soundings from the ASTEX flights, it was determined that this level corresponds well with the height of the solid-cloud top (see examples in Figures 13 and 14). The red-colored region at the top of the image represents the inversion layer and the free atmosphere. The interfacial, gradient layer in-between is the entrainment zone.

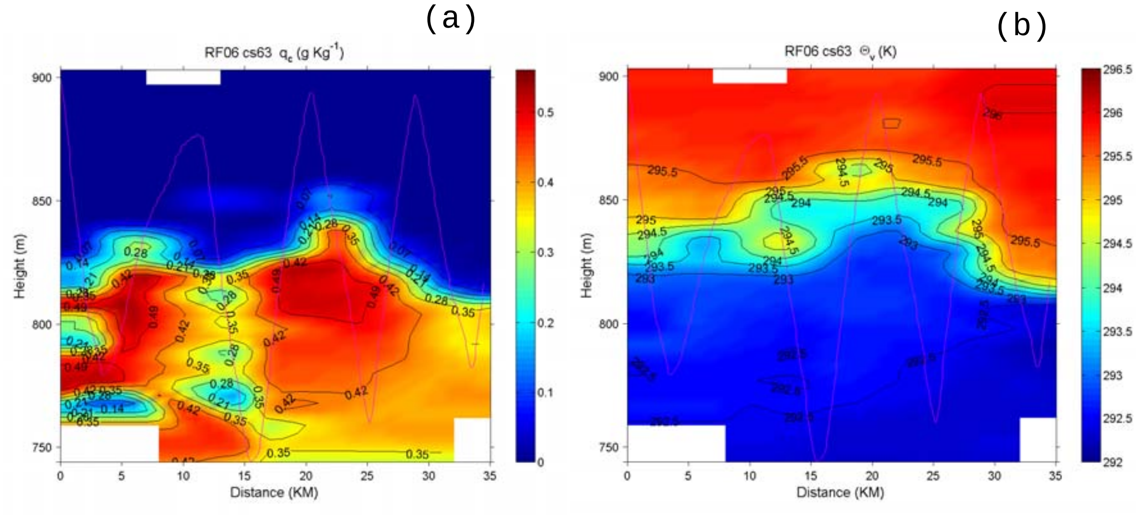

Figure 24. Same as in Figure 23, except for RF06.

During RF06, two solid cloud protrusions at 7 km and 23 km distance from the starting point can be identified (Figure 24a). The depth of these cloud protrusions appears to be smaller than those in RF05 (Figure 23a), however, the presence of residual cloud droplets above the solid-cloud top appear to be more widespread, even above the cloud-top troughs. The temperature profile (Figure 24b) shows a broad entrainment zone in the wispy cloud region with a depth of 20 to 30 m. In addition, cloud liquid water content below the cloud ridges appears to be significantly enhanced (maximum q_c is about 0.5 g kg^{-1}), as opposed to that found in the cloud troughs (approximately 0.2 g kg^{-1}). Compared to the profiles observed from RF05, the cloud ridges appear to have larger spatial scales and are coherent with inner boundary-layer dynamics.

Two vertical cross sections were obtained from RF07. The first cross section shows significant sloping of the cloud-top layer. It changes from 1160 to 970 m within a 40-km distance (Figure 25a). Cloud-top soundings from this region indicate that the droplet size below the deep cloud region (the first 20 km of the leg) is larger, approximately 22 μm, and gradually decreases to 16 μm at the end of the leg. Hence, it is possible that the high cloud top at the beginning of the leg is a result of mesoscale convective activity. However, further analyses are needed to verify this hypothesis.

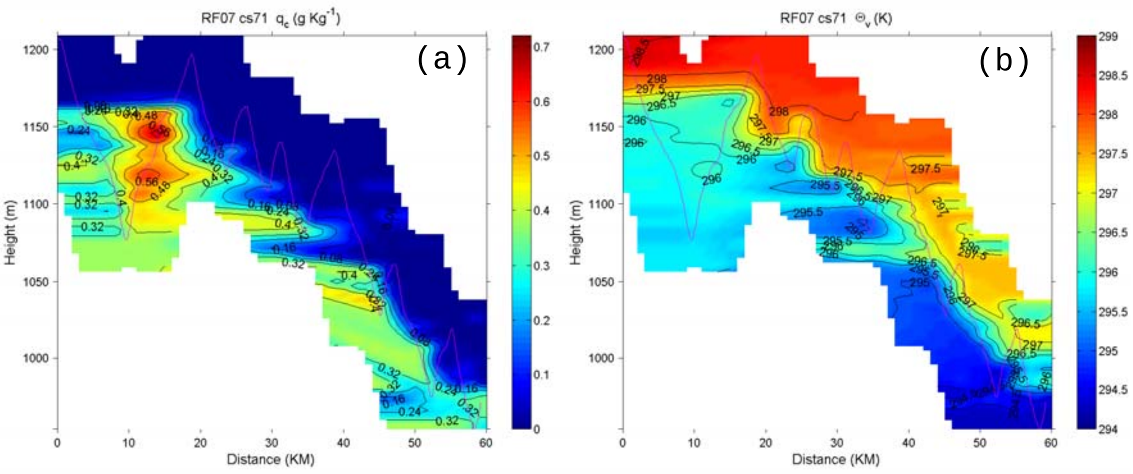

Figure 25. Same as in Figure 23, except for cross section #1 of RF07.

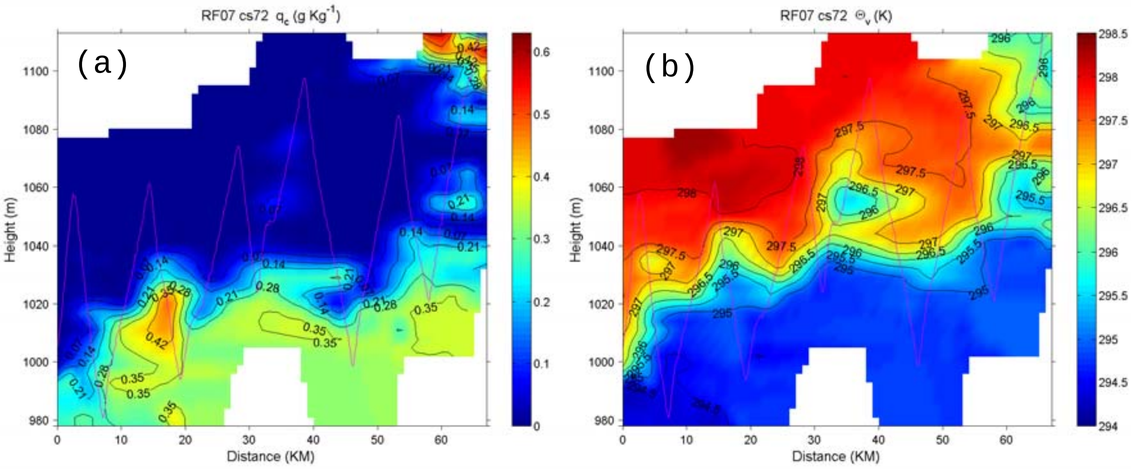

Figure 26. Same as in Figure 23, except for cross section #2 RF07.

Figure 26 shows the results from the second cross section of RF07. This figure reveals the same magnitude of cloud-top variations as seen in the previous figure, but with more scattered cloud protrusions. Some residual cloud droplets are seen between 30 and 40 km from the starting point of the leg, and deeper protrusions of cloud are seen at 60 km into the leg. Figure 27 shows the corresponding ozone concentration levels from the same zigzag leg. Here, a large region approximately 40 km from the start of the leg indicates ozone levels with boundary-layer properties to 1090 m above sea level. Thus, this implies that the wispy cloud droplets seen in Figure 26a are all that remain of a previously penetrating cloud extending to about 1090 m.

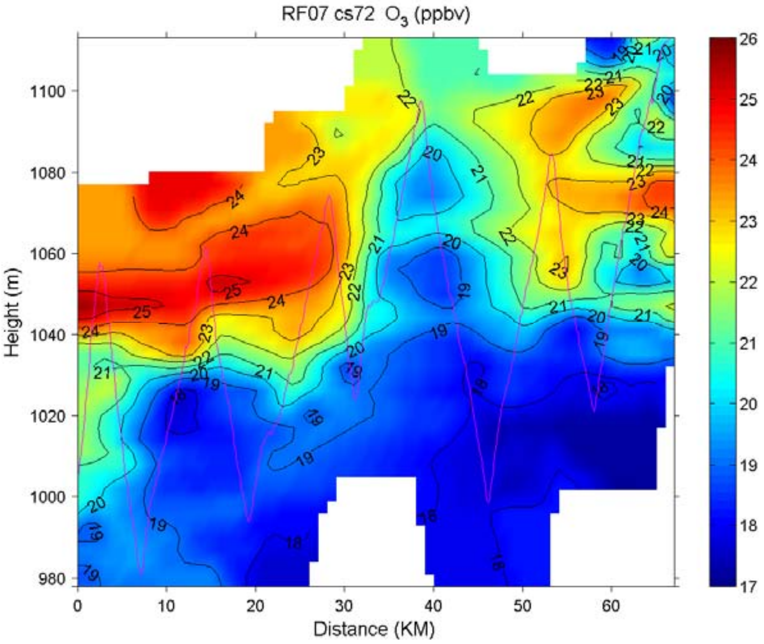

Figure 27. Same as in Figure 26, except for ozone concentration (ppbv).

With cool SSTs, the protrusions of cloud into the inversion layer occur on a relatively small scale (5-10 km), as seen during RF05. With warmer SSTs, these protrusions appear to be larger in scale (15-20 km) and possibly coupled with the thermodynamics of the surface-mixed layer. In addition, a deep entrainment zone with detectable cloud droplets was found only above the cloud ridges over cool water. Entrainment zones over warmer water were more widespread and shallower.

3. Properties of the Entrainment Zone

From the myriad soundings of all three Lagrangian IOP I flights, many entrainment zones were observed. They were easily identified in regions where large temperature variations existed above the solid-cloud top. The main characteristic of this layer is strong temperature variation with a weak temperature inversion at its base. This layer may also contain strong variations in water vapor or ozone and may sometimes contain a small number of cloud droplets. The bottom of the entrainment zone is usually located at the solid-cloud top, below which little variation of temperature is seen (see Figure 14).

a. Height Measurements

Extensive measurements of individual layer heights were made for each of the Lagrangian IOP I flights (see Tables 2 – 4). These measurements included the height of the boundary-layer top, the entrainment-zone top, the top of strong turbulence perturbations, and the top of weak turbulence perturbations. The depth of the entrainment zone was determined by subtracting the entrainment-zone top from the boundary-layer top. When the top of an individual layer could not be found due to bad or insufficient data, the placeholder “NaN” was inserted to indicate “not a number.”

The cloud-top flight legs are numbered sequentially. Soundings with large vertical depths were designated as “LL” for long legs.

Table 2. RF05 layer heights.

Leg	Boundary layer top (m)	Entrainment zone top (m)	Depth of entrainment zone (m)	Strong turbulence top (m)	Weak turbulence top (m)
1	722	735	13	735	740
2	716	730	14	726	NaN
3	714	726	12	724	NaN
4	721	727	6	732	NaN
5	741	756	15	753	NaN
6	730	735	5	735	751
7	725	730	5	726	733
8	714	720	6	718	NaN
9	714	726	12	733	743
10	727	731	4	733	NaN
11	735	737	2	739	747
12	726	729	3	725	734
13	755	766	11	757	764
14	749	765	16	747	777
15	754	755	1	755	774
16	750	754	4	749	778
17	762	789	27	760	768
18	736	757	21	746	759
19	753	762	9	751	784
20	743	773	30	742	779
21	771	797	26	772	796
22	755	773	18	775	NaN
23	738	765	27	739	NaN
24	760	761	1	762	769
25	764	773	9	760	774
26	765	767	2	732	772
LL1	563	568	5	563	578
LL2	686	690	4	692	762
LL3	477	481	4	482	572
LL4	501	NaN	NaN	479	NaN
LL5	676	681	5	635	718

Table 3. RF06 layer heights.

Leg	Boundary layer top (m)	Entrainment zone top (m)	Depth of entrainment zone (m)	Strong turbulence top (m)	Weak turbulence top (m)
1	652	655	3	651	659
2	646	661	15	636	NaN
3	685	687	2	685	NaN
4	672	678	6	680	687
5	689	704	15	691	NaN
6	687	NaN	NaN	710	NaN
7	734	736	2	735	NaN
8	710	742	32	710	742
9	749	NaN	NaN	754	NaN
10	NaN	NaN	NaN	NaN	NaN
11	730	740	10	739	NaN
12	744	756	12	740	762
13	743	746	3	743	749
14	755	756	1	757	785
15	802	816	14	818	NaN
16	788	791	3	791	NaN
17	NaN	NaN	NaN	NaN	NaN
18	836	NaN	NaN	837	NaN
19	917	976	59	975	995
20	906	943	37	944	967
21	884	910	26	912	927
22	822	860	38	851	870
23	825	837	12	838	857
24	819	854	35	818	NaN
25	829	863	34	839	NaN
26	840	866	26	866	NaN
27	832	861	29	847	866
28	810	815	5	820	833
29	812	842	30	842	877
30	818	856	38	858	871
31	837	897	60	894	NaN
32	854	870	16	869	885
33	838	851	13	838	862
34	791	811	20	812	839
35	770	781	11	783	805
36	764	792	28	766	797
37	760	771	11	761	781
38	773	780	7	770	787
39	786	791	5	787	808
40	724	745	21	729	761
41	742	747	5	739	751
42	769	776	7	770	791
LL5	752	776	24	769	NaN
LL6	NaN	NaN	NaN	NaN	NaN

Table 4. RF07 layer heights.

Leg	Boundary layer top (m)	Entrainment zone top (m)	Depth of entrainment zone (m)	Strong turbulence top (m)	Weak turbulence top (m)
1	1161	1172	11	1159	1183
2	1170	1175	5	1175	1184
3	1140	1143	3	1142	1159
4	1139	1156	17	1156	NaN
5	1116	1117	1	1117	1137
6	1116	1118	2	1118	NaN
7	1095	1113	18	1114	1127
8	1103	1111	8	NaN	NaN
9	1078	1099	21	NaN	NaN
10	1036	1049	13	1050	NaN
11	1012	1034	22	1027	1043
12	996	1001	5	1005	1008
13	979	999	20	990	1006
14	1000	1041	41	1015	1033
15	1019	1036	17	1036	1050
16	1018	1032	14	1020	NaN
17	1034	1046	12	1036	NaN
18	1023	1030	7	1027	1053
19	1039	1049	10	1037	1058
20	1040	1078	38	1071	1083
21	1033	1060	27	1036	1061
22	1027	1045	18	1036	1056
23	1046	1050	4	1043	1051
LL1	1081	1087	6	1080	1097
LL2	955	1092	137	951	NaN
LL3	1093	1188	95	1195	1250
LL4	1097	1298	102	1114	NaN
LL5	1092	1123	30	1096	1177
LL6	858	968	110	NaN	NaN
LL7	1151	1195	44	1155	1180

The top of the boundary layer was determined by locating the top of the cloud-mixed layer. Droplet concentration number and droplet size often gave clear indications of the extent of the solid-cloud top. Well-mixed regions in the temperature and ozone profiles also helped identify the boundary-layer top. The top of the entrainment zone was resolved by looking for the sharp inversion base of the free atmosphere in the temperature, specific humidity, and ozone soundings. The extent of strong turbulence was determined by identifying where perturbations significantly diminished on the w′ (vertical motion perturbations) profiles. A similar process was repeated for weak turbulence signatures. The w′ profiles were followed from the top of the highest strong turbulence signature up to the height where laminar flow began. An example of how this technique was executed follows.

Figure 28 is a sounding from Research Flight 5, leg 5. These soundings reveal a boundary-layer top which rises to an altitude of 755 m. The base of the free-atmosphere inversion layer is located at 766 m. Thus, the entrainment zone has a depth of 11 m. Turbulence perturbations in the wind field were categorized as strong, weak, or non-turbulent. Strong turbulence signatures can be seen up to 757 meters. Weak turbulence perturbations attenuate sharply 2 meters below the entrainment-zone top. The results from all of the Lagrangian IOP I flights can be seen in Figures 29 – 31. These figures summarize the findings from Tables 2 – 4.

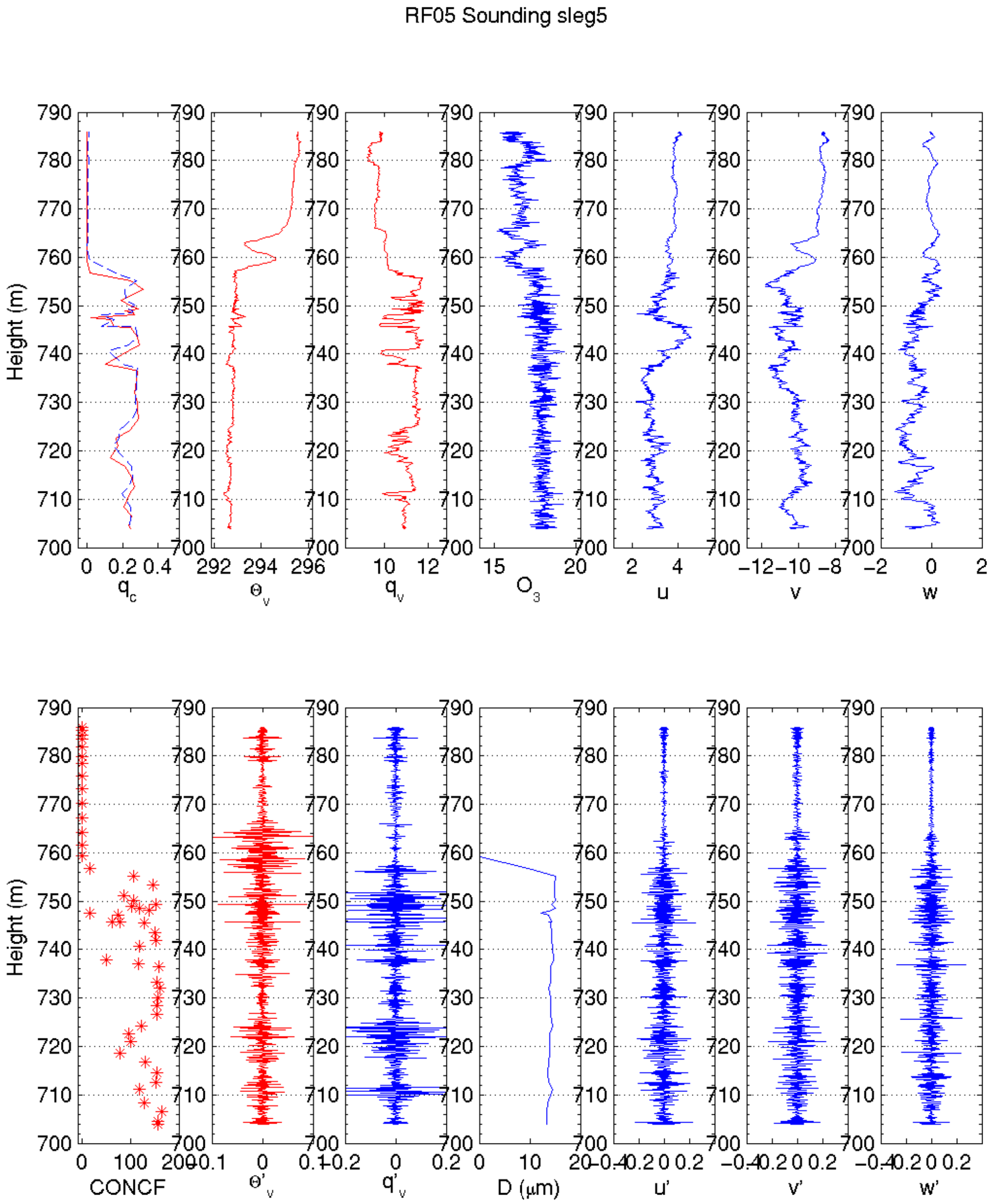

Figure 28. Same as Figure 12, except for Research Flight 5, leg 5. The top of the boundary layer is at 755 m; the strong turbulence top is at 757 m; the weak turbulence top is at 764 m; the interfacial-layer top is at 766 m; the entrainment-zone depth is 11 m.

Figure 29 is a scatter-plot diagram which compares the height of the solid-cloud top to the extent of the strong turbulence layer top. According to the classical view of boundary-layer dynamics, the domain of turbulence should end at the cloud top due to the presence of a stable, capping layer of air (Stull 1988, p. 13). Interestingly, strong turbulence extended above the solid-cloud top in many cases. However, a correlation was found between inversion-layer strength and the extent of strong turbulence. The stronger the inversion layer, the shallower the depth of the strong turbulence layer. Research Flight 5 had the strongest inversion layers due to the robust subsidence found at higher latitudes. Thus, turbulence signatures for this flight corresponded well with the height of the BL.

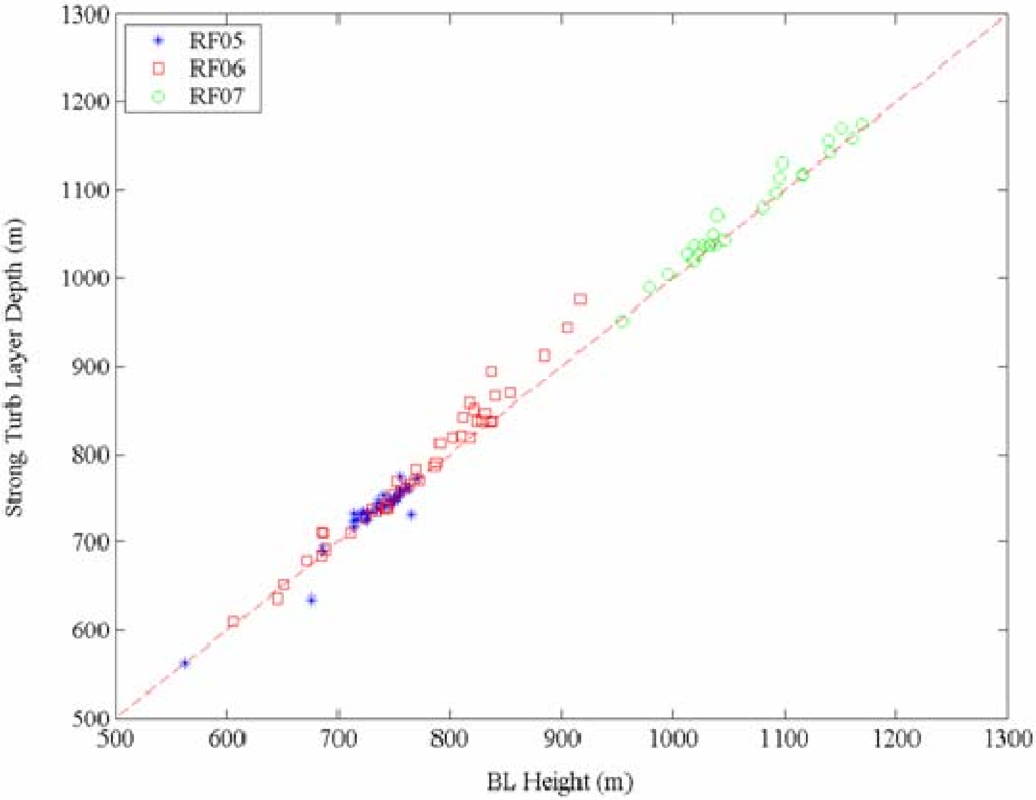

Figure 29. A scatter-plot diagram of boundary-layer height versus the depth of the strong turbulence layer during Lagrangian IOP I. The upper limit of strong turbulence generally ends just above the top of the boundary layer.

Figure 30 compares the extent of weak turbulence to the height of the solid-cloud top. Regions of weak turbulence persisted, on average, 30 m or more above the cloud-mixed layer for all three flights. Above the inversion layer, turbulence was difficult to discern as the free atmosphere became dominated by laminar flow. Figure 31 reveals a linear relationship between weak turbulence height and the top of the entrainment zone. Turbulence signatures dissipate at or below the top of the entrainment-zone region. Therefore, the weak turbulence layer and the entrainment zone are synonymous.

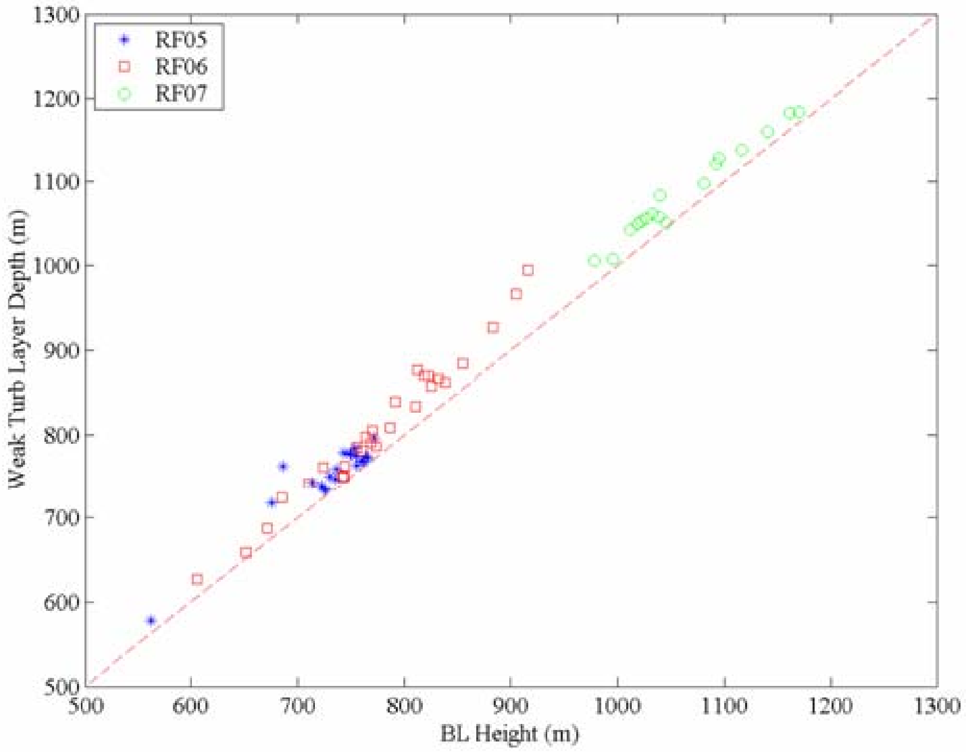

Figure 30. A scatter-plot diagram of boundary-layer height versus the depth of the weak turbulence layer during Lagrangian IOP I. This diagram illustrates that the upper limit of weak turbulence extends tens of meters above the top of the boundary layer. This region corresponds well to the length scale of the entrainment zone.

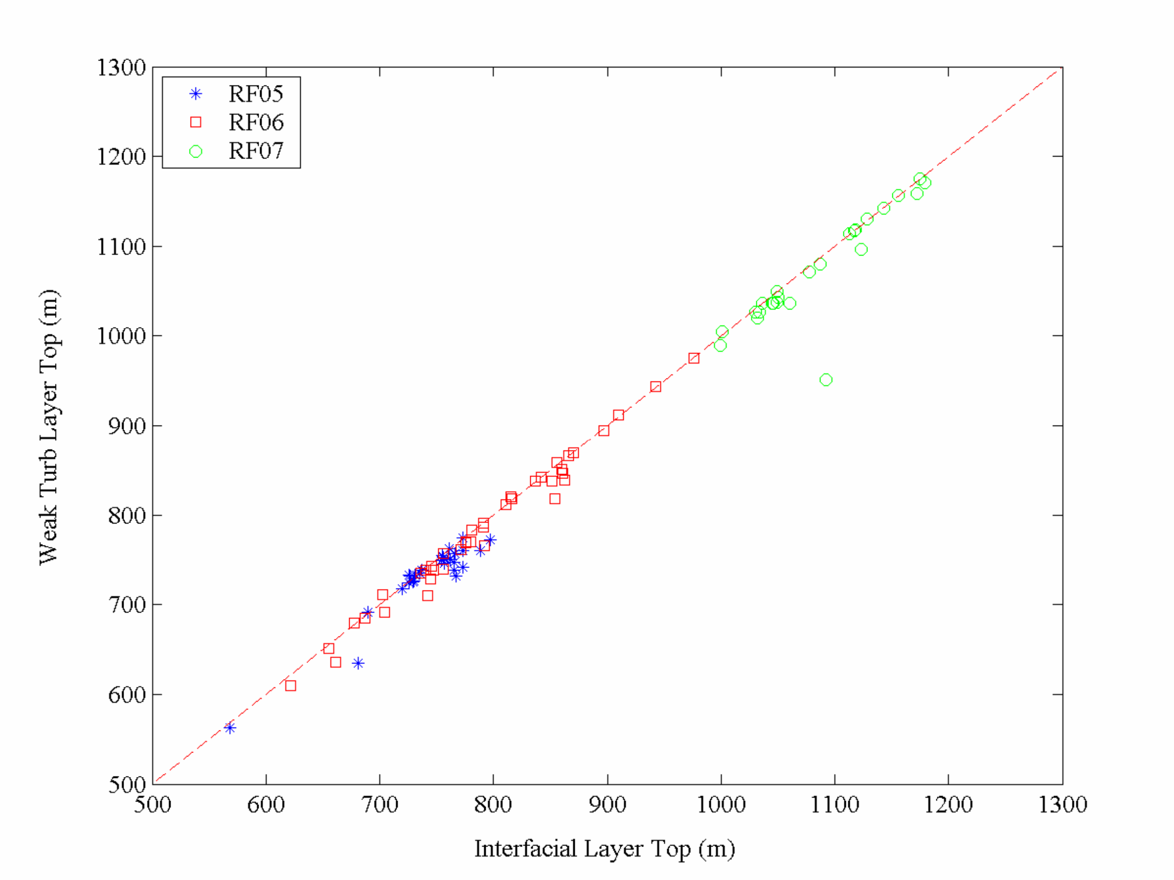

Figure 31. A scatter-plot diagram of interfacial-layer (entrainment-zone) height versus the depth of the weak turbulence layer during Lagrangian IOP I. This diagram illustrates that weak turbulence signatures dissipate at or near the top of the entrainment zone.

b. Mixing-line Analyses

Mixing-line analyses were performed to further interrogate turbulent mixing in the entrainment zone. This technique provides a way of measuring how much autonomy individual parcels retain in the entrainment zone. This technique is outlined in further detail by Lenschow et al. (2000).

The soundings in Figure 32 reveal an entrainment zone that is approximately 38 m deep, from 905 to 943 m.

Figure 33a characterizes the air located in the vicinity of the entrainment zone. The blue circles on the left-hand side of the mixing line indicate 100 percent boundary-layer air. The smaller red circles on the right-hand side of the diagram represent 100 percent free-atmosphere air. The green dots in-between indicate entrainment-zone air. A larger concentration of entrainment-zone air is located near the top of the mixing line. This indicates that the entrainment-zone parcels have a greater distribution of boundary-layer-like air. The probability histogram in Figure 33b provides the same results--the air in the entrainment zone contains a greater fraction of boundary-layer air.

Figure 34 is a sounding approximately 40 km downstream from Figure 32. The entrainment zone in this example is approximately 25 m deep. The mixing line (Figure 35a) indicates that most of the air in this entrainment zone resembles free-atmosphere air. The same results are indicated on the probability histogram in Figure 35b. These results conflict with the assessment from the previous mixing-line analysis and histogram (Figure 33).

Upon further study, it became evident that entrainment-zone mixing was a time-evolving process. The greater the lapse in time from the start of entrainment mixing, the greater the probability that air in the entrainment zone will have the characteristics of free-atmosphere air. On the other hand, the smaller the time lapse, the higher the chance air parcels will resemble boundary-layer air in the entrainment zone. Further evidence for these conclusions can be found in the soundings from Figures 32 and 34. The temperature sounding in Figure 34 distinctly indicates the existence of an entrainment zone at approximately 825 to 850 m. The liquid water sounding, however, reveals virtually cloud-free air. Conversely, significant liquid water amounts can be found in the entrainment zone of Figure 32. In addition, turbulence signatures from the wind components are higher here than in Figure 34. Thus, the entrainment zone in Figure 32 displays more boundary-layer-air characteristics than the entrainment zone seen in Figure 34. This implies that Figure 32 is in an earlier stage of dissipation, while Figure 34 is in a later stage.

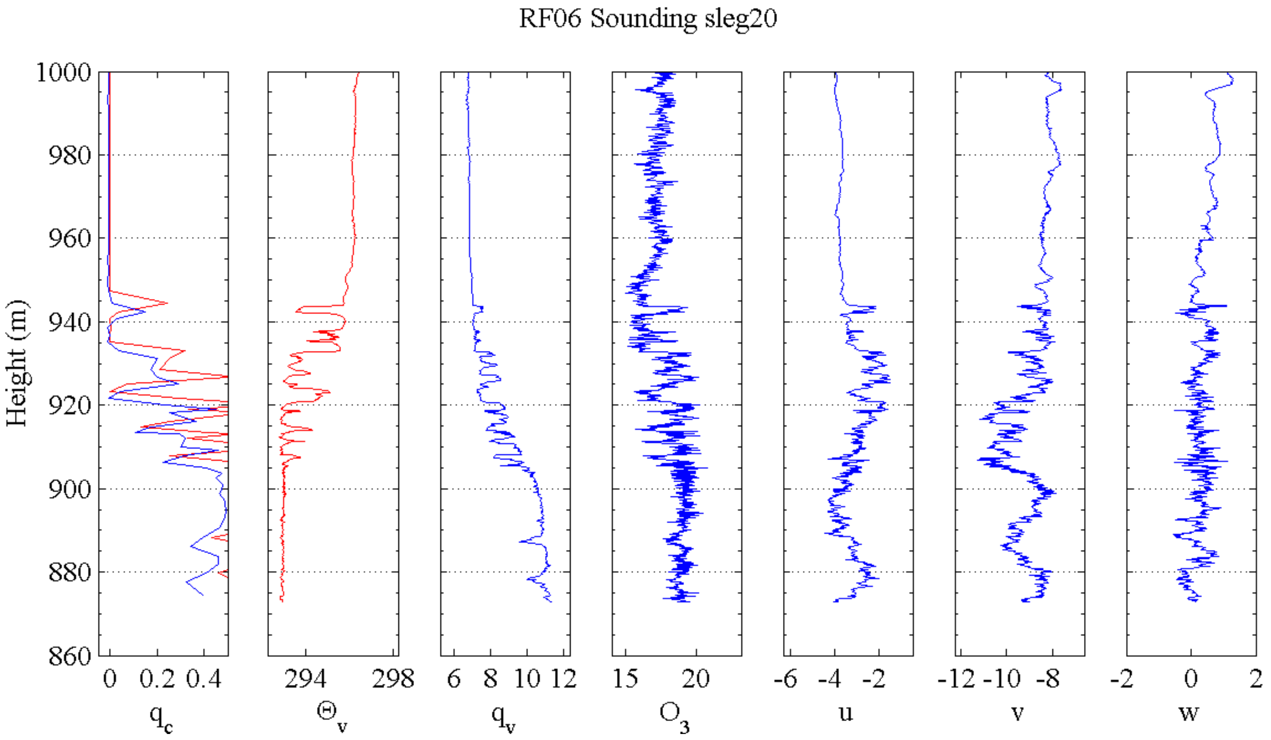

Figure 32. Same as in Figures 12a - 12g, except for Research Flight 6, leg 20.

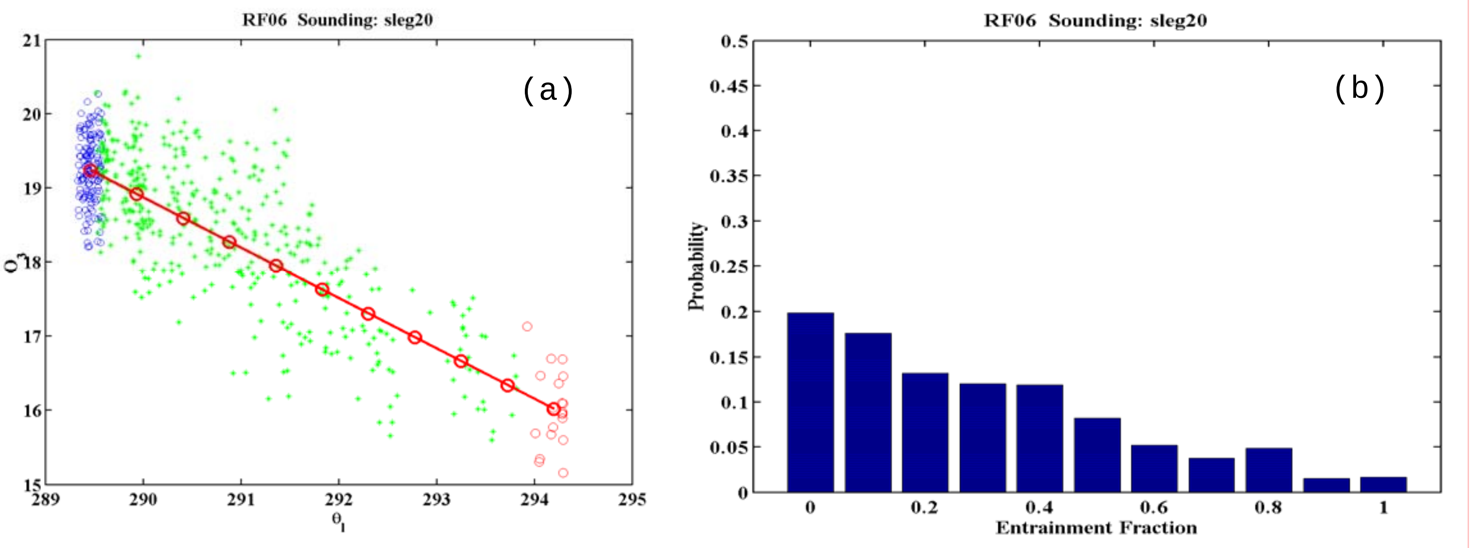

Figure 33. (a) Mixing line analysis for Research Flight 6, leg 20. (b) Probability histogram for Research Flight 6, leg 20.

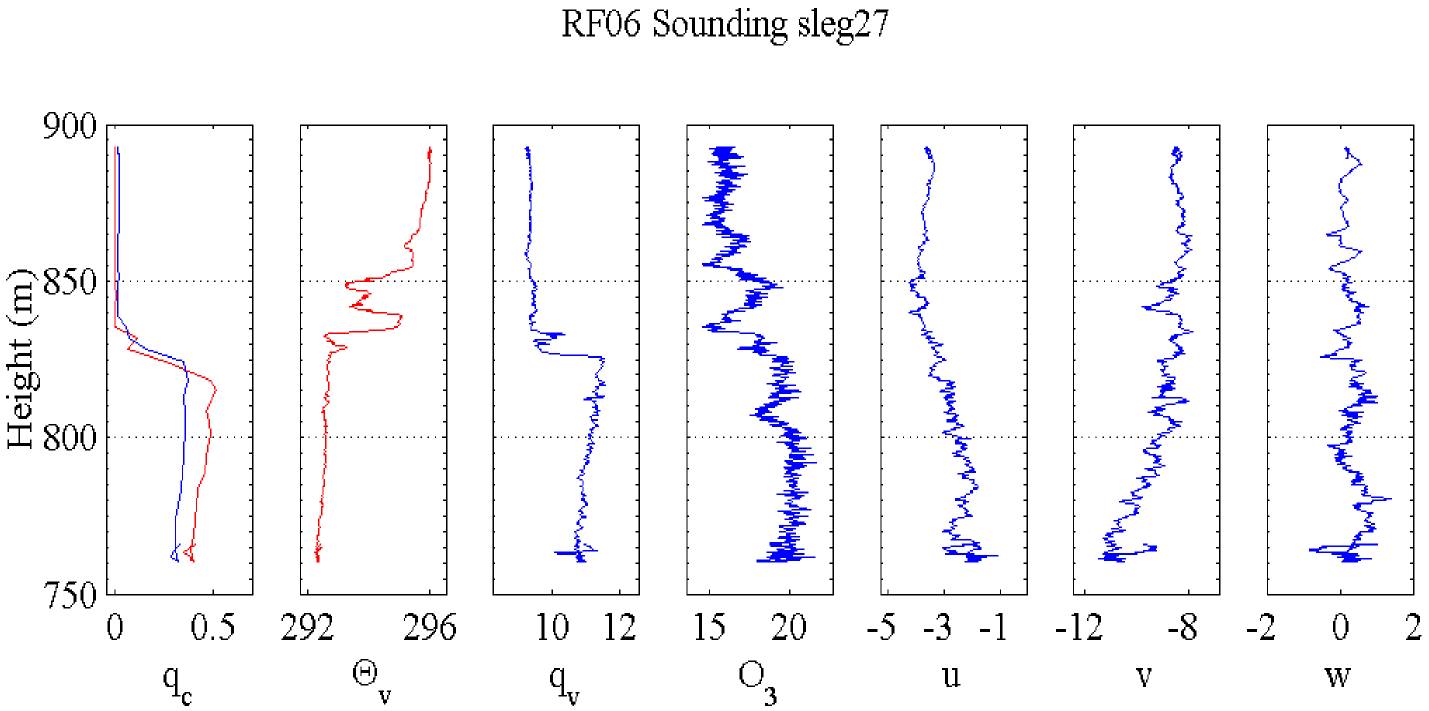

Figure 34. Same as in Figures 12a - 12g, except for Research Flight 6, leg 27.

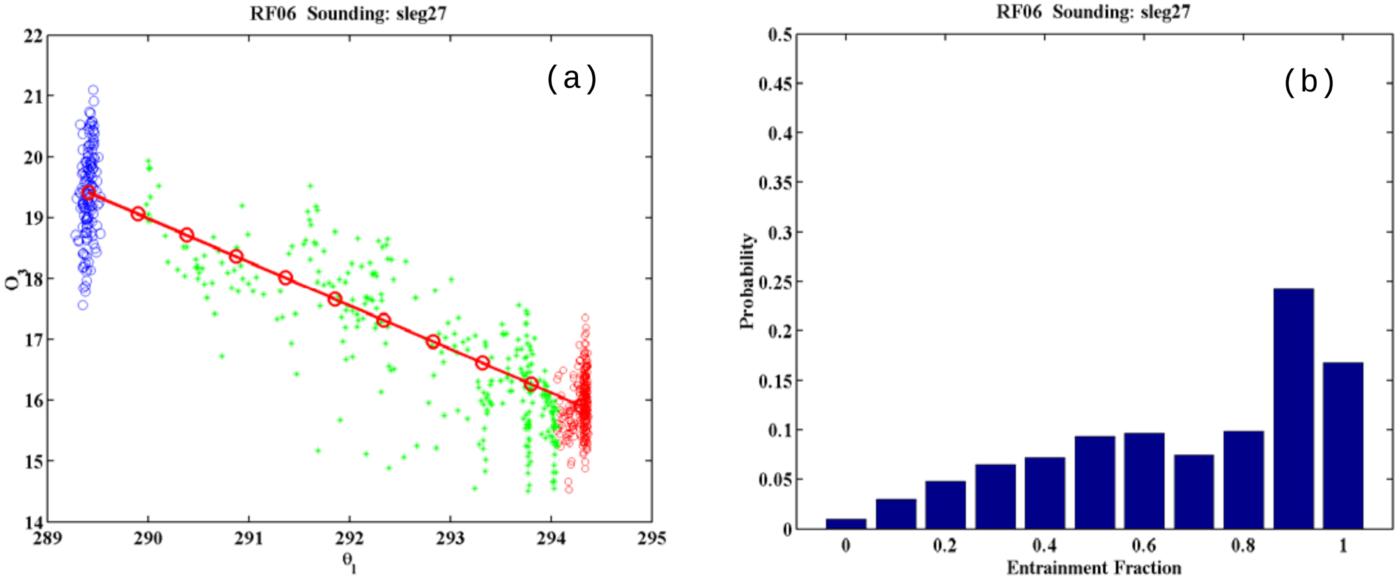

Figure 35. (a) Mixing line analysis for Research Flight 6, leg 27. (b) Probability histogram for Research Flight 6, leg 27.

c. Vertical Cross Sections

Vertical cross sections can also be used to determine the characteristics of entrainment-zone mixing. In Figure 36a, wispy cloud matter (i.e., low liquid water content) is present above the solid-cloud top at approximately 30 km into the flight at a height of 1060 m. Based solely on the data from Figure 36a, it is difficult to determine if the wispy clouds are the result of new clouds forming or the dissipation of an older cloud. However, when the corresponding temperature and ozone cross sections are interrogated, it becomes clear that the wispy cloud region is most certainly in the process of dissipation. The temperature and ozone fields in the same corresponding area resemble a gradient structure similar to the solid-cloud top, which marks the top of the boundary layer. These profiles reveal that the wispy cloud region is in the final stages of dissipation. As liquid water dissipated, the cloud vanished, but the temperature and ozone signatures with boundary-layer-air characteristics remained behind. Thus, the implication drawn from these results is that mixing in the entrainment zone dissipates the upper-cloud layer.

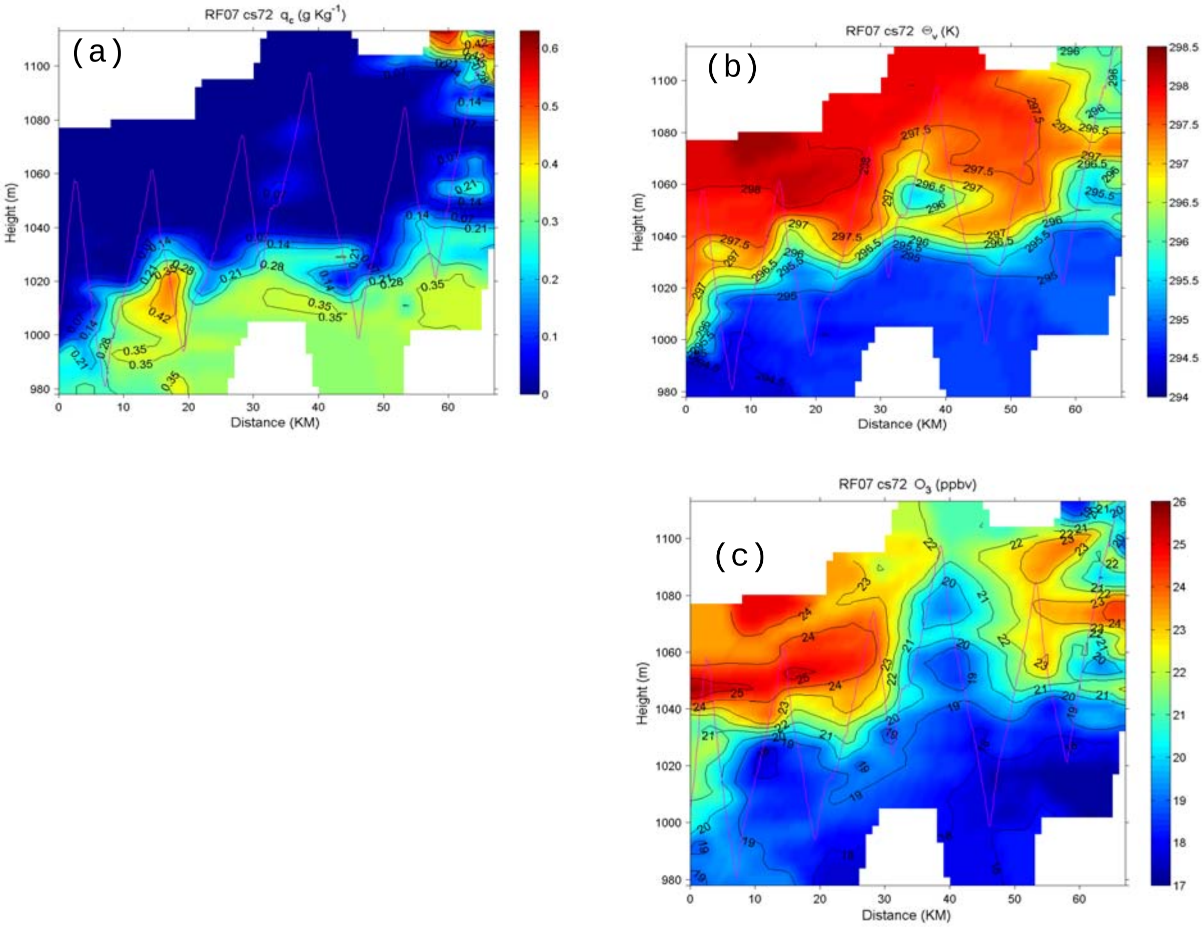

Figure 36. Same as in Figure 21, except for cross section #2 of Research Flight 7. (a) liquid water content (g kg^{-1})(b) virtual potential temperature (K). (c) ozone (ppbv).

IV. DISCUSSION

A. SUMMARY AND CONCLUSIONS

The major objectives of this thesis were to characterize entrainment-zone structure using fine-scale aircraft measurements, and to understand the impact of cloud-top entrainment on cloud evolution. Cloud-top parameterizations can be further developed through a better awareness of entrainment-zone processes. Fine-scale measurements made during ASTEX by NCAR’s Electra aircraft were used in this study. A general analysis of entrainment-zone structure included all 17 of Electra’s flights, but the main thrust of this thesis concentrated on flights 5, 6, and 7. These flights conducted measurements from a Lagrangian frame of reference. This method can track individual air parcels over the course of their trajectory, without any time discontinuities. An in-depth analysis of the measurements obtained during ASTEX revealed characteristics about cloud-top structure that have not been reviewed in previous literature.

The vertical cross sections examined in this study indicate that the cloud tops observed during ASTEX are not uniform in appearance. The cloud-top surface undulates as a series of troughs and ridges. Variations were also apparent in cloud-top gradients. For example, the thermal gradient in cloud-top ridges was often steeper than those observed in cloud-top troughs. Incorporating these gradient differences into cloud-top parameterizations may prove useful. It should be noted, however, that only a limited number of samples were viewed and further statistical analysis is needed to confirm these findings.

Layered structure above the solid-cloud top was a common feature in many of the analyzed soundings. These layers were typically 10 to 30 meters thick and resided immediately above the top of the mixed layer. According to the classical view of boundary-layer structure, the inversion layer should begin at the top of the mixed layer. This was not the case in most of the analyzed soundings. The inversion layer was frequently found several to tens of meters above the mixed-layer top. Current entrainment parameterizations use jump conditions at the mixed-layer top, which may not be appropriate given that the sharp inversion base during this study was found above the top of the mixed layer.

The classical boundary-layer viewpoint also suggests that turbulence does not persist above the mixed-layer top, due to a stable, capping layer of air. However, this study consistently observed the presence of turbulence well beyond the peak of the mixed layer. Turbulence did decrease in magnitude above the top of the mixed layer, but weak turbulence signatures persisted tens of meters above the mixed-layer top. Furthermore, the top of the weak turbulence height corresponded to the top of the entrainment zone.

The presence of turbulence and a complex, layered structure above the solid-cloud top suggest that the top of the boundary layer is not collocated with the top of the mixed layer. This idea is supported by Lenschow et al. (2000) in their study of marine stratocumulus clouds off the California coast. Mixing in both studies was observed to occur several meters above the cloud top. The air immediately above the mixed layer was once the solid-cloud top, but it is now in the process of dissipation due to entrainment. As the cloud droplets evaporate, the height of the solid-cloud top decreases and an additional layer forms as the residual turbulence decays. This results in the formation of a new entrainment zone, and the existence of these layers is a reflection of the history of the cloud-top’s evolution.

To interrogate turbulent mixing further, mixing-line analyses were performed. The results of these analyses revealed that entrainment-zone mixing is a time-evolving process. The greater the time lapse since the onset of entrainment at the cloud top, the greater the amount of cloud dissipation, and vice versa. In other words, the longer entrainment mixing occurs, the more the entrainment zone will resemble free-atmosphere air.

Vertical cross sections provided further evidence to corroborate this hypothesis. When wispy cloud regions were viewed by focusing solely on liquid water content, it was difficult to determine if the wispy clouds were in the process of forming or dissipating. However, when compared with corresponding temperature and ozone profiles (from both the aircraft soundings and the vertical cross sections) it was easy to distinguish between cloud formation and cloud dissipation. As liquid water dissipates, the cloud vanishes, but temperature, ozone, and wind signatures with boundary-layer-air characteristics remain behind. Thus, the implication is that entrainment-zone mixing dissipates the upper-cloud layer. However, continuous dissipation of the upper-cloud layer has not been observed. Further study is needed to examine the interaction between entrainment and the full integration of boundary-layer dynamics (e.g., boundary-layer circulations).

B. RECOMMENDATIONS FOR FUTURE RESEARCH

The findings of this study offer intriguing insight on entrainment-zone and boundary-layer processes using a limited number of soundings. However, inconsistencies in the data suggest room for improvement. A simple way to improve upon the results of this study would be to produce or examine larger data sets for statistical analysis. A clearer and better-substantiated view of entrainment-zone processes could be obtained by interrogating more data.

To obtain a cohesive view of boundary-layer structure and evolution, several observational platforms should be employed. A more comprehensive view of boundary-layer processes will unfold by combining *in situ* aircraft measurements with other observational tools such as satellite imagery, rawinsondes, and cloud radars. Instead of relying solely on measurements from one platform, an ensemble of platforms would provide the most complete picture of the boundary layer to date.

Finally, the results of this thesis should be cross-examined with the outcome of other studies, to determine universal applicability of the boundary-layer processes identified in this study. For example, the cloud-topped boundary layers along the eastern Atlantic may have different characteristics than those found in the eastern Pacific. Recent field studies such as DYCOMS-II (Dynamics and Chemistry of Marine Stratocumulus Phase II; Stevens et al. 2003) and EPIC (East Pacific Investigation of Climate Processes in the Coupled Ocean-Atmosphere System; Bretherton et al. 2004) should offer valuable insight on boundary-layer structure and processes. The Global Energy and Water Cycle Experiment (GEWEX) Cloud System Study (GCSS) Boundary Layer

Cloud Working Group has forthcoming plans to conduct a series of model intercomparison studies based on both EPIC and DYCOMS-II (Bretherton et al. 2004). Comparisons with older studies such as FIRE (First International Satellite Cloud Climatology Project Regional Experiment; Albrecht et al. 1988) should not be neglected, however. These studies also contain vast amounts of information and detail about the boundary layer still waiting to be discovered.

THIS PAGE INTENTIONALLY LEFT BLANK

LIST OF REFERENCES

Ahrens, C. D., 1994: *Meteorology Today: An Introduction to Weather, Climate, and the Environment*. 5th ed. West Publishing Company, 591 pp.

Albrecht, B. A., D. A. Randall, and S. Nicholls, 1988: Observations of marine stratocumulus clouds during FIRE. *Bull. Amer. Meteor. Soc*., **69**, 618-626.

———, C. S. Bretherton, D. Johnson, W. H. Scubert, and A. S. Frisch, 1995: The Atlantic stratocumulus transition experiment—ASTEX. *Bull. Amer. Meteor. Soc*., **76**, 889-904.

Bach, W. D., Jr., and R. S. Harmon/ARO (Army Research Office), Army Research Laboratory, cited 1999: 1999 ARO in review: Environmental sciences. [Available online at http://www.aro.army.mil/arorev99/enviro99.htm], Access date - November 2004.

Bretherton, C. S., and R. Pincus, 1995: Cloudiness and marine boundary layer dynamics in the ASTEX lagrangian experiments. Part I: Synoptic setting and vertical structure. *J. Atmos. Sci*., **16**, 2707-2723.

———, P. Austin, and S. T. Siems, 1995: Cloudiness and marine boundary layer dynamics in the ASTEX lagrangian experiments. Part II: Cloudiness, drizzle, surface fluxes, and entrainment. *J. Atmos. Sci*., **16**, 2724-2751.

———, T. Uttal, C. W. Fairall, S. E. Yuter, R. A. Weller, D. Baumgardner, K. Comstock, R. Wood, and G. B. Raga, 2004: The EPIC 2001 stratocumulus study. *Bull. Amer. Meteor. Soc*., **85**, 967-977.

Glickman, T. S. (Managing Ed.), 2000: *Glossary of Meteorology*. 2d ed. American Meteorological Society, 855 pp.

Gregory, G. L., B. E. Anderson, M. A. Owens, and W. R. Cofer, cited 2002: P3-B *in situ* ozone measurements. [Available online at http://www-gte.larc.nasa.gov/pem/gregory_p3bInst.htm], Access date - October 2004.

Jonsson, H./Chief Research Scientist, Center for Interdisciplinary Remotely Piloted Aircraft Studies (CIRPAS), Naval Postgraduate School (NPS), 2004.

Kogan, Y. L., M. P. Khairoutdinov, D. K. Lilly, Z. N. Kogan, and Qingfu Liu, 1995: Modeling of stratocumulus cloud layers in a large eddy simulation model with explicit microphysics. *J. Atmos. Sci*., **16**, 2923-2940.

Lenschow, D. H., Ed., 1986: *Probing the Atmospheric Boundary Layer*. American Meteorological Society, 269 pp.

———, M. Zhou, X. Zeng, L. Chen, and X. Xu, 2000: Measurements of fine-scale structure at the top of marine stratocumulus. *Boundary-Layer Meteorology*, **97**, 331-357.

McDowell, D. W., 1999: Determining entrainment rate and the role of entrainment in stratocumulus clouds. M.S. thesis, Department of Meteorology, Naval Postgraduate School, 67 pp.

Randall, D. A., 1995: Editorial, Atlantic stratocumulus transition experiment. *J. Atmos. Sci*., **16**, 2705.

———, cited 2004: Atlantic stratocumulus transition experiment. [Available online at http://kiwi.atmos.colostate.edu/scm/astex.html.], Access date - June 2004.

RAF (Research Aviation Facility), NCAR (National Center for Atmospheric Research), cited 2002: Bulletin No. 4, The NSF/NCAR ELECTRA (N308D): Overview and summary of capabilities. [Available online at http://raf.atd.ucar.edu/Bulletins/bulletin4.html.], Access date - October 2004.

———, cited 2000: Bulletin No. 22, Airborne humidity measurements. [Available online at http://www.atd.ucar.edu/raf/Bulletins/bulletin22.html.], Access date - October 2004.

———, cited 2001: Bulletin No. 23, Measurement techniques: Air motion sensing. [Available online at http://www.atd.ucar.edu/raf/Bulletins/bulletin23.html.], Access date - October 2004.

———, cited 1989: Bulletin No. 24, Forward Scattering Spectrometer Probe. [Available online at http://raf.atd.ucar.edu/Bulletins/B24/fssp100.html.], Access date - October 2004.

Ruth, R. L./Earth Observing Laboratory, NCAR, cited 1996: NCAR airborne instrumentation inventory. [Available online at http://www.atd.ucar.edu/dir_off/airborne/102E2AL.html.], Access date - October 2004.

Sears, F. W., M. W. Zemansky, and H. D. Young, 1987: *University Physics*. 7th ed. Addison-Wesley Publishing Company, 1096 pp.

Stevens, B., W. R. Cotton, G. Feingold, and C. H. Moeng, 2003: Dynamics and chemistry of marine stratocumulus—DYCOMS-II. *Bull. Amer. Meteor. Soc.*, **84**, 579-593.

Stull, R. B., 1988: *An Introduction to Boundary Layer Meteorology*. Kluwer Academic Publishers, 670 pp.

Wang, Q., and D. H. Lenschow, 1995: An observational study of the role of penetrating cumulus in a marine stratocumulus-topped boundary layer. *J. Atmos. Sci.*, **16**, 2778-2787.

Warren, S., C. J. Hahn, J. London, R. M. Chervin, and R. L. Jenne, 1989: Global distribution of total cloud cover and cloud type amounts over the ocean. NCAR Tech. Note TN-317+STR, 150 pp.

THIS PAGE INTENTIONALLY LEFT BLANK

INITIAL DISTRIBUTION LIST

1. Defense Technical Information Center
   Ft. Belvoir, Virginia

2. Dudley Knox Library
   Naval Postgraduate School
   Monterey, California

3. Professor Qing Wang
   Department of Meteorology
   Naval Postgraduate School
   Monterey, California

4. Professor “Chuck” Wash
   Department of Meteorology
   Naval Postgraduate School
   Monterey, California

5. Professor Philip A. Durkee
   Department of Meteorology
   Naval Postgraduate School
   Monterey, California

6. Dr. Keith G. Blackwell
   Department of Earth Sciences
   University of South Alabama
   Mobile, Alabama

7. Capt Robb M. Randall
   Department of Atmospheric Sciences
   University of Arizona
   Tucson, Arizona

8. Capt Daniel L. Weekley
   2 OSS/OSW
   Barksdale AFB, Louisiana

9. GS-11 Mary B. Horner
   HQ Air Combat Command/DOXF
   Langley AFB, Virginia

10. MSgt (R) Jerry Horner
    13238 Blue Mesa Court
    Victorville, California